Mechanical Systems and Signal Processing 255 (2026) 114450

Contents lists available at ScienceDirect

Mechanical Systems and Signal Processing

journal homepage: www.elsevier.com/locate/ymssp

Full length article

Homotypic multi-source joint representation with dynamic hierarchical feature tracing in hybrid Walsh–frequency domain for prior knowledge-constrained fault diagnosis of multi-cylinder drilling pumps

Peng Chen [a,b], Yazheng Wang [a], Yuhao Wu [a], Yaqiang Jin [c], Changbo He [d,*], Ge Xin [e]

[a] *College of Engineering, Shantou University, Shantou, 515063, Guangdong, PR China*
[b] *Key Laboratory of Intelligent Manufacturing Technology, Ministry of Education, Shantou, 515063, Guangdong, PR China*
[c] *School of Qilu Transportation, Shandong University, Jinan, 250061, Shandong, PR China*
[d] *School of Electrical Engineering and Automation, Anhui University, Hefei, 230601, PR China*
[e] *School of Traffic and Transportation, Beijing Jiaotong University, Beijing, 100044, PR China*

ARTICLE INFO

Communicated by D. Yurchenko

Keywords:
Multi-cylinder drilling pumps
Multi-source
Signal processing
Faults diagnosis
Prognostics and health management

ABSTRACT

Fault diagnosis in multi-cylinder drilling pumps is fundamentally challenged by homotypic multi-source mixing, where identical mechanical mechanisms generate overlapping spectral signatures that obscure early fault indicators. Contemporary state-of-the-art methods often falter in these complex environments, lacking the stability to maintain performance across varying pressure levels and the sensitivity to quantify the severity and urgency of developing faults. To address these limitations, this study proposes the Homotypic Multi-source joint Representation with Dynamic Hierarchical Feature Tracing (HMR-DHFT) framework. The methodology integrates a prior-independent energy-kurtosis screening mechanism for adaptive mode reconstruction, a hybrid Walsh–frequency feature space to resolve spectral blurring, and a matrix-free dynamic ridge tracking algorithm to extract fault evolution patterns. Experimental validation confirms that the proposed framework achieves superior diagnostic resolution and reliability when compared to recent state-of-the-art approaches and domain-specific baselines. Key results demonstrate that HMR-DHFT not only achieves superior fault isolation accuracy across four distinct operating pressure regimes but also successfully characterizes the severity and urgency of failures—capabilities that are notably absent in existing signal processing baselines. These findings establish the framework as a robust solution for monitoring complex mechanical systems under diverse hydraulic operational conditions.

1. Introduction

In the field of modern drilling operations, multi-cylinder drilling pumps function as indispensable circulating equipment, whereby their design enables them to serve as the cornerstone of fluid management systems [1–3]. These highly specialized pumps are engineered to efficiently transport high-pressure drilling fluid through an intricate circulating manifold to reach the wellbore's bottom, thereby simultaneously accomplishing multiple critical objectives: maintaining optimal drill bit temperature through cooling

---

* Corresponding author.
E-mail addresses: pengchen@alu.uestc.edu.cn (P. Chen), changbh@ahu.edu.cn (C. He).

https://doi.org/10.1016/j.ymssp.2026.114450
Received 6 February 2026; Received in revised form 13 April 2026; Accepted 15 May 2026

mechanisms, ensuring thorough bit cleansing, executing comprehensive wellbore bottom purification, facilitating the systematic removal of rock cuttings, and crucially, maintaining the delicate equilibrium of formation pressure. However, despite their robust engineering, the fluid end, which acts as the primary pressure boosting module for drilling fluid, frequently encounters operational challenges, particularly in the form of suction and discharge valve malfunctions when subjected to complex and harsh working environments. Consequently, the implementation of timely and accurate fault diagnosis protocols for the fluid end has emerged as a matter of paramount importance, not only for ensuring the continuous and efficient progression of drilling operations but also for substantially minimizing the probability of safety-related incidents.

The reported methods for fault diagnosis and predictive maintenance in drilling pumps systems predominantly rely on manual inspections, which are heavily influenced by the subjective expertise and experience of engineers. While previous research [4–9] has explored the use of vibration signals to diagnose faults and extract features in mechanical equipment, challenges remain due to the complexity of dynamic behaviors exhibited by system components such as bearings, gears, valves, and pistons during failure. These components exhibit failure dynamics that are intrinsically tied to characteristic frequencies, including rotational and pump stroke frequencies, emphasizing the importance of extracting fault-related features from vibration signals, particularly under non-stationary operating conditions. In the domain of drilling pumps, the power end and fluid end generate a multitude of vibration sources, coming from mechanisms such as piston and connecting rod motion, force patterns that correlate with crankshaft angles, and environmental noise including transient disturbances [10–12]. The vibration signals captured in both normal and faulty states are characterized by distinctive periodic time-domain properties, which propagate through diverse transmission paths to sensors, resulting in multi-source mixed signals. These signals are influenced by factors such as mixed convolution, signal modulation, transmission path characteristics, and the underlying motion mechanisms, leading to significant non-linearity, non-stationarity, and other intricate attributes. As emphasized in a recent comprehensive review by Omidali et al. [13], reciprocating equipment like piston engines and pumps demonstrates inherently complex dynamic behaviors due to cyclic variations, making the development of robust fault indicators that can detect subtle deviations from normal operational patterns a critical and ongoing challenge. Consequently, identifying specific impulse sources within these complex signals and accurately extracting their time–frequency domain features have become critical challenges in the fault diagnosis, health condition monitoring, and localization of faults in drilling pumps, representing a crucial area of ongoing research in the field.

In the field of mechanical fault diagnosis and detection, particularly for complex drilling pump systems, addressing the challenges of identifying multi-source signals and extracting fault-related features remains a critical and demanding task requiring advanced analytical methods. These challenges have spurred significant research efforts, leading to the development of diverse theoretical frameworks and methodologies, which utilize key signal attributes such as spectral characteristics, statistical independence, sparsity, and spatial distribution variations to achieve enhanced fault detection outcomes. As a result, several innovative signal processing techniques have emerged, with Wavelet Transform (WT) [14], Empirical Mode Decomposition (EMD) [15], Variational Mode Decomposition (VMD) [16], and Impulsive Mode Decomposition (IMD) [17] standing out as prominent approaches, each offering unique capabilities for decomposing and analyzing complex mechanical signals [18–20]. These techniques, when applied strategically, enable a comprehensive understanding of fault characteristics and contribute to advancing predictive maintenance strategies in mechanical systems.

Highlighting specific advancements, Dragomiretskiy et al. [16] proposed a non-recursive Variational Mode Decomposition model that overcomes the limitations of traditional methods like Empirical Mode Decomposition by concurrently extracting modes based on a narrow-band prior. This method demonstrates improved robustness to noise and sampling, theoretical soundness, and computational efficiency. To further address the limitations of data preprocessing in dynamic processes, Zhang et al. [21] recently proposed an enhanced VMD model optimized by the Harris Hawk algorithm. This approach significantly improves the detection of minor faults in industrial systems by adaptively optimizing mode numbers and penalty terms, demonstrating the potential of optimized decomposition in complex environments.

Hou et al. [17] introduced Impulsive Mode Decomposition (IMD), a novel decomposition method tailored for adaptive extraction of pulse components. By formally defining impulsive modes, establishing a geometrically-mean-based pq-mean for quantification, and employing an iteratively-searching adaptive filterbank, IMD excels in isolating impulsive components from complex signals. This approach surpasses existing techniques in various applications, including machinery fault diagnosis and ECG denoising. Moreover, Yang et al. [22] designed a decision fusion framework that couples mode decomposition with evidence theory for improved fault diagnosis accuracy during drilling processes. This approach breaks down raw data into frequency-centered series, reconstructs them into groups, and applies local diagnostic models, integrating results with weight-based evidence theory fusion to account for frequency variations across fault modes. This method effectively enhances diagnostic performance in complex scenarios.

Li et al. [23] developed a fault diagnosis method for drilling pump fluid ends by combining a 1D-to-3D signal expansion operation with a modified AlexNet convolutional neural network (CNN). This method enhances feature visibility, reduces noise, and achieves a mean accuracy of 98.00% across nine fault types, outperforming existing techniques and marking a significant step forward in fault diagnosis methodologies. Similarly, Guo et al. [24] addressed the need for efficient maintenance in drilling pumps by introducing a deep feature learning method. Their approach, which combines CNNs with Transformer networks in parallel channels, effectively extracts both time–frequency and time-domain features to predict remaining useful life, further validating the efficacy of deep learning in this specific domain.

Together, these contributions underscore the growing sophistication and effectiveness of modern approaches in addressing complex mechanical fault detection challenges. Building on these advancements, Li et al. [25] introduced a maximum time-shift kurtosis-based method (MTSK-HMMS-S) to address the challenge of separating homotypic multi-source mixed signals in reciprocating drilling pumps. By integrating the pump's motion mechanism and prior stroke frequency parameters, the method adaptively extracts and decouples cyclic impulse sequences, enhancing diagnostic accuracy and localization through the implementation of a Vibration Grading Weighted Index (VGWI).

In real-world industrial scenarios, where signal mixing and homotypic source complexity have become increasingly challenging, conventional signal decomposition methods have shown significant limitations in their applicability and effectiveness. This complexity is further exacerbated by noise and outlier disturbances in multisource sensor signals. Addressing this, Zhang et al. [26] developed a unified tensor-based classifier that converts noisy multisource signals into time–frequency tensor samples. This method effectively mines coupled structural information to improve diagnostic robustness, highlighting the importance of advanced spatial–temporal analysis in noisy industrial settings.

Consequently, modern analytical approaches require a fundamental shift toward examining the intrinsic and distinctive characteristics of signals as their primary starting point. This approach is particularly evident in the field of reciprocating machinery, such as drilling pumps, where operational dynamics naturally generate periodic impulse signals that serve as crucial indicators of component degradation and failure. Furthermore, ensuring the trustworthiness and interpretability of these diagnostic models is becoming paramount. Xu et al. [27] recently proposed a physics-informed probabilistic deep network that integrates physical labels with fault data. This approach not only captures accurate fault characteristics but also enhances the interpretability of the diagnostic process, suggesting a trend toward methods that combine data-driven power with physical mechanism constraints. Given this intricate relationship between signal characteristics and mechanical health conditions, the development and implementation of sophisticated techniques for precise extraction of these periodic impulse signatures has emerged as a vital cornerstone in the broader framework of equipment fault detection and diagnostic protocols, thereby establishing a critical bridge between signal processing theory and practical maintenance applications.

In recent advancements within machinery fault diagnosis, several innovative approaches have emerged to enhance feature extraction and fault detection capabilities. Notably, Miao et al. [28] developed the coarse-to-fine minimum entropy deconvolution (CFMED) method, which significantly improves upon traditional MED through its novel two-stage initialization and filtering strategy, thereby enabling more precise extraction of fault-induced impulses in rotating machinery. Building upon this progress, the same research group [29] further advanced the field by introducing the deep network-based maximum correlated kurtosis deconvolution method (MCKD-DeNet), which integrates Hanning window filter initialization with a pioneering cost function based on correlated kurtosis, alongside autocorrelation-guided input period estimation. This integrated approach has demonstrated remarkable superiority over existing deconvolution methods in both simulated and real-world bearing fault diagnosis scenarios. Complementing these developments, Guo et al. [30] proposed an adaptive symplectic geometric mode decomposition (SGMD) method, incorporating cycle kurtosis entropy (CKE) for weak feature extraction and compound fault detection. Their method's innovative use of CKE for optimizing sliding window length and component selection has substantially enhanced SGMD's decomposition and denoising capabilities under challenging noise conditions. Furthermore, Lu et al. [31] contributed to this evolving landscape by introducing the maximum average kurtosis morphological deconvolution (MAKMD) method, which synergistically combines enhanced time-varying morphological filtering (ETVMF) with diagonal slice spectrum analysis. This comprehensive approach not only effectively suppresses random impulse interference but also facilitates clearer coupling frequency identification, ultimately achieving superior performance in both simulated and practical fault diagnosis applications.

Despite significant advances in vibration analysis methodologies for fault detection in reciprocating mechanical equipment, particularly in drilling pump systems, several fundamental challenges persist and warrant comprehensive investigation.

1. Contemporary signal decomposition techniques, such as standard VMD, fundamentally demand empirical pre-setting of crucial parameters like mode numbers. In dynamic drilling operations characterized by varying pressure regimes, this reliance on static prior parameters often leads to over-decomposition or mode mixing, severely restricting automated deployment and diagnostic robustness.
2. While recent studies have explored homotypic source separation, they predominantly rely on purely spectral decoupling. These approaches often falter because identical mechanical structures in multi-cylinder pumps generate overlapping resonance bands, causing transient fault impulses to dissolve into background noise and lose their distinctive spectral characteristics.
3. Advanced Blind Source Separation (BSS) algorithms theoretically address multi-source mixing by estimating complex mixing matrices. However, in reciprocating equipment, fault-induced impulsive features are intrinsically sparse and lack precise prior knowledge. This sparsity, combined with the statistically consistent nature of homotypic mixed signals, makes accurate mixing matrix estimation mathematically ill-posed and exceptionally vulnerable.

In response to these multifaceted challenges, this investigation introduces a novel methodological framework: the Homotypic Multi-source joint Representation with Dynamic Hierarchical Feature Tracing (HMR-DHFT) in the hybrid Walsh–frequency domain, specifically designed for prior knowledge-constrained fault diagnosis of multi-cylinder drilling pumps. This innovative approach leverages the fundamental motion mechanism of triplex drilling pumps in conjunction with prior knowledge of pump stroke frequency to facilitate the automatic separation of impulse sequences from multiple cylinders within the original vibration signals. Through this sophisticated integration of mechanical principles and signal processing techniques, the HMR-DHFT method enables effective capturing of different fault characteristics, thereby offering a more robust and accurate diagnostic capability. The significance of this methodological advancement is underscored by its potential to address the aforementioned challenges in vibration analysis and fault detection, particularly in complex mechanical systems where traditional approaches have shown limitations. The main contributions of this paper are summarized as follows:

1. **An adaptive, prior-independent, and parameter-insensitive modal reconstruction method:** Unlike standard VMD which strictly relies on prior knowledge for the manual selection of the mode number K and penalty factor α, we introduce a dual-constraint energy-kurtosis screening mechanism. This approach automatically isolates stroke-related vibration modes from background noise. More importantly, it demonstrates exceptional robustness to parameter variations, effectively overcoming the reliance on empirical tuning and mitigating spectral overlapping in homotypic mixing.
2. **Hybrid Walsh–frequency feature representation:** To resolve the lack of distinct spectral characteristics in multi-source signals, we construct a high-dimensional joint feature space. By fusing frequency-domain periodicity with sequency-domain discontinuity detection, this method selectively amplifies the abrupt transients of mechanical impacts, thereby enhancing the discriminability of subtle fault impulses that are otherwise obscured in traditional time–frequency domains.
3. **Matrix-free dynamic feature tracing:** We propose a gradient-based ridge tracking framework that treats the feature map as a topographic surface. This eliminates the need for complex mixing matrix estimations common in BSS, allowing for the direct extraction and severity quantification of fault evolution patterns from sparse signals.

The structure of this manuscript is organized as follows: Section 2 lays the foundational groundwork for this research, providing the necessary preliminaries and context. The detailed explanation of the proposed framework, which focuses on homotypic multi-source joint representation and dynamic hierarchical feature tracing within the hybrid Walsh–frequency domain, is presented in Section 3. Multiple experimental validations, designed to demonstrate the effectiveness and robustness of the framework, are comprehensively discussed in Section 4. Finally, the conclusions and key findings of this study are summarized in Section 5, highlighting the broader implications and potential future directions.

2. Preliminaries

Variational Mode Decomposition (VMD) [16] constitutes an approach within the field of signal processing, specifically designed for signal decomposition and estimation. By iteratively solving an optimization problem derived from a variational framework, VMD adaptively partitions the frequency domain of a given signal. This procedure not only facilitates a systematic subdivision of the signal into distinct frequency bands, but also enables the effective isolation of individual components. Through this iterative search for the optimal solution, the method accurately identifies both the frequency center and the bandwidth associated with each mode, thereby ensuring precise and efficient component separation.

Given a signal $f(t) \in L^2(\mathbb{R})$, the fundamental objective of VMD is to systematically decompose this signal into a predetermined number of K distinct modes, denoted as $\{u_k(t)\}_{k=1}^{K}$, whereby each mode is uniquely characterized by its corresponding center frequency ω_k and exhibits a finite bandwidth. The underlying optimization principle seeks to minimize the aggregate bandwidth of all constituent modes while simultaneously ensuring that their superposition closely approximates the original input signal. This comprehensive decomposition process, which balances mode separation with signal reconstruction fidelity, can be mathematically formulated as an optimization problem.

$$\min_{\{u_k\},\{\omega_k\}} \sum_{k=1}^{K} \left\| \partial_t \left(u_k(t) * e^{-j\omega_k t} \right) \right\|_{L^2}^2 \qquad \text{s.t.} \qquad \sum_{k=1}^{K} u_k(t) = f(t) \tag{1}$$

where ∂_t represents the time derivative, and $\|\cdot\|_{L^2}$ is the L^2 norm, quantifying the bandwidth of each mode.

To address the constrained problem, a quadratic penalty term $\boldsymbol{\omega}$ and a Lagrangian multiplier $\lambda(t) \in L^2(\mathbb{R})$ are introduced to enforce the reconstruction constraint. The unconstrained Lagrangian is expressed as:

$$\mathcal{L}(\{u_k\},\{\omega_k\},\lambda) = \sum_{k=1}^{K} \left\| \partial_t \left(u_k * e^{-j\omega_k t} \right) \right\|_{L^2}^2 + \alpha \left\| f(t) - \sum_{k=1}^{K} u_k(t) \right\|_{L^2}^2 - \left\langle \lambda(t), f(t) - \sum_{k=1}^{K} u_k(t) \right\rangle \tag{2}$$

where $\langle \cdot , \cdot \rangle$ signifies the inner product in $L^2(\mathbb{R})$.

The optimization is solved iteratively using the Alternating Direction Method of Multipliers (ADMM), which updates each mode $\hat{u}_k$, its center frequency ω_k and the Lagrangian multiplier $\hat{\lambda}$ sequentially:

$$\hat{u}_k^{n+1}(\omega) = \frac{\hat{f}(\omega) - \sum_{i<k} \hat{u}_i^{n+1}(\omega) - \sum_{i>k} \hat{u}_i^{n}(\omega) + \frac{\hat{\lambda}^n(\omega)}{2}}{1 + 2\alpha(\omega - \omega_k^n)^2} \tag{3}$$

$$\omega_k^{n+1} = \frac{\int_0^\infty \omega |\hat{u}_k^{n+1}(\omega)|^2 d\omega}{\int_0^\infty |\hat{u}_k^{n+1}(\omega)|^2 d\omega} \tag{4}$$

$$\hat{\lambda}^{n+1}(\omega) = \hat{\lambda}^n(\omega) + \tau \left(\hat{f}(\omega) - \sum_k \hat{u}_k^{n+1}(\omega) \right) \tag{5}$$

The iterative process will continue until convergence is reached, which is determined by the following formula:

$$\sum_k \frac{\left\| \hat{u}_k^{n+1} - \hat{u}_k^n \right\|_{L^2}^2}{\left\| \hat{u}_k^n \right\|_{L^2}^2} < \epsilon \tag{6}$$

In VMD, practitioners must carefully pre-define four key parameters: the mode number K, the bandwidth control parameter α, the noise tolerance τ, and the convergence tolerance ϵ. While τ and ϵ typically have minimal influence and are assigned default values, α plays a critical role in balancing noise suppression and mode smoothness, requiring careful tuning. The selection of K is particularly challenging, especially without prior signal knowledge. An excessively high K can cause over-decomposition, generating redundant modes and reducing interpretability. Conversely, too low a K may lead to mode mixing, merging intrinsic signal components and compromising frequency fidelity.

3. The proposed methodology of homotypic multi-source joint representation framework with dynamic hierarchical feature tracing in hybrid Walsh–frequency domain

The construction of the proposed framework is fundamentally driven by specific prior knowledge regarding the physical mechanism of reciprocating compressor valve faults. Physically, early-stage valve faults manifest as quasi-periodic transient impulses that excite high-frequency structural resonances, resulting in non-stationary modulation signatures in the vibration signal. To formally integrate this prior knowledge, we mathematically formalized these characteristics into a two-stage processing strategy. First, the algorithm assumes the signal is composed of sparse, band-limited modes, utilizing Variational Mode Decomposition to isolate the impulsive resonance components in the frequency domain. Second, the periodicity and structural characteristics of the fault impacts are formalized through the Ridge Line Score, which models the fault signature as a continuous energy trajectory in the joint frequency-Walsh domain. By calculating the cumulative energy along these theoretical ridge paths, the method transforms the physical detection of periodic impacts into a mathematical maximization problem, thereby ensuring diagnostic specificity and robustness against background interference.

However, the direct application of standard algorithms to realize this formalization encounters practical obstacles. While Variational Mode Decomposition (VMD) provides a robust basis for signal analysis, its reliance on a preset mode number K and sensitivity to noise pose significant hurdles for diagnosing multi-cylinder drilling pumps. These issues are compounded by the spectral indistinguishability of homotypic sources and the challenges of estimating mixing matrices for sparse signals. To resolve these limitations, this study proposes the HMR-DHFT framework, as illustrated in Fig. 1. The methodology is structured as follows: Section 3.1 introduces a statistical energy-kurtosis approach to adaptively reconstruct variational modes without manual parameter tuning. Section 3.2 constructs a hybrid Walsh–frequency feature space to differentiate spectrally overlapping components. Finally, Section 3.3 details a dynamic ridge tracking mechanism to extract fault features directly from the joint representation.

3.1. *Adaptive reconstruction of specific variational modes: A statistical energy-kurtosis approach for complex mechanical systems*

Homotypic multi-source signals in multi-cylinder pumps exhibit high temporal periodicity and overlapping resonance bands, making separation via traditional spectral analysis difficult. This complexity arises from the combined influence of equivalent transmission pathways due to structural symmetry, precise temporal synchronization between sources, and complex coupling effects resulting from rigid interconnections.

To address these challenges, the methodology begins with the establishment of a comprehensive mathematical framework for stroke frequency analysis. To precisely characterize the periodic nature of the pump operation, we establish a set of target frequencies Ω_{stroke} corresponding to the fundamental stroke rate f_0 and its significant harmonics. This set serves as a reference for identifying relevant vibrational modes:

$$\Omega_{\text{stroke}} = \{f_0, 2f_0, \dots, n_{\max} f_0\}, \quad f_0 = \frac{1}{T_s} \tag{7}$$

where T_s represents the fundamental stroke cycle duration, characterizing the temporal requirements for a complete mechanical work cycle, and $n_{\max}$ denotes the predetermined highest harmonic order considered in the analysis.

Following the initial frequency domain characterization, a quantitative evaluation mechanism is implemented to assess the correlation between each Intrinsic Mode Function (IMF), derived through VMD decomposition using default parameters, and the target frequency components. We quantify the relevance of each IMF by calculating an energy ratio coefficient η_k. This metric assesses the proportion of spectral energy concentrated within the target harmonic bands relative to the total energy, thereby distinguishing stroke-related dynamics from broadband noise:

$$\eta_k = \frac{\sum_{b=1}^{B} \int_{f_b-\Delta f}^{f_b+\Delta f} \left|\hat{u}_k(\omega)\right|^2 \mathrm{d}\omega}{\int_0^{\infty} |\hat{u}_k(\omega)|^2 \mathrm{d}\omega}, \quad f_b \in \Omega_{\text{stroke}}, \quad \Delta f = f_0/3 \tag{8}$$

where η_k approaches unity when the mode's energy is dominated by the pump's mechanical rotation frequencies, indicating a high correlation with the physical motion mechanism.

Subsequently, by calculating the kurtosis in the harmonic band, the time-domain impulse characteristics of the signal can be effectively extracted when the energy ratio coefficient cannot fully characterize the signal. The screening index κ_k, defined as the maximum harmonic band kurtosis, is calculated as follows:

$$\kappa_k = \max_{b=1}^{B} \left\{ \frac{\mathbb{E}[(u_k^b(t) - \mu_k^b)^4]}{(\mathbb{E}[(u_k^b(t) - \mu_k^b)^2])^2} - 3 \right\}, \quad u_k^b(t) = \mathrm{Re}\left\{ \mathcal{F}^{-1}\left\{ \hat{u}_k(\omega) \cdot \mathrm{rect}\left(\frac{\omega - f_b}{\Delta f}\right) \right\} \right\} \tag{9}$$

where κ_k represents the quantified impulsive feature of the kth IMF, derived by maximizing the kurtosis calculated across B harmonic bands. $u_k^b(t)$ denotes the real-valued filtered signal of the kth IMF in band b, obtained by taking the real part (Re) of the inverse

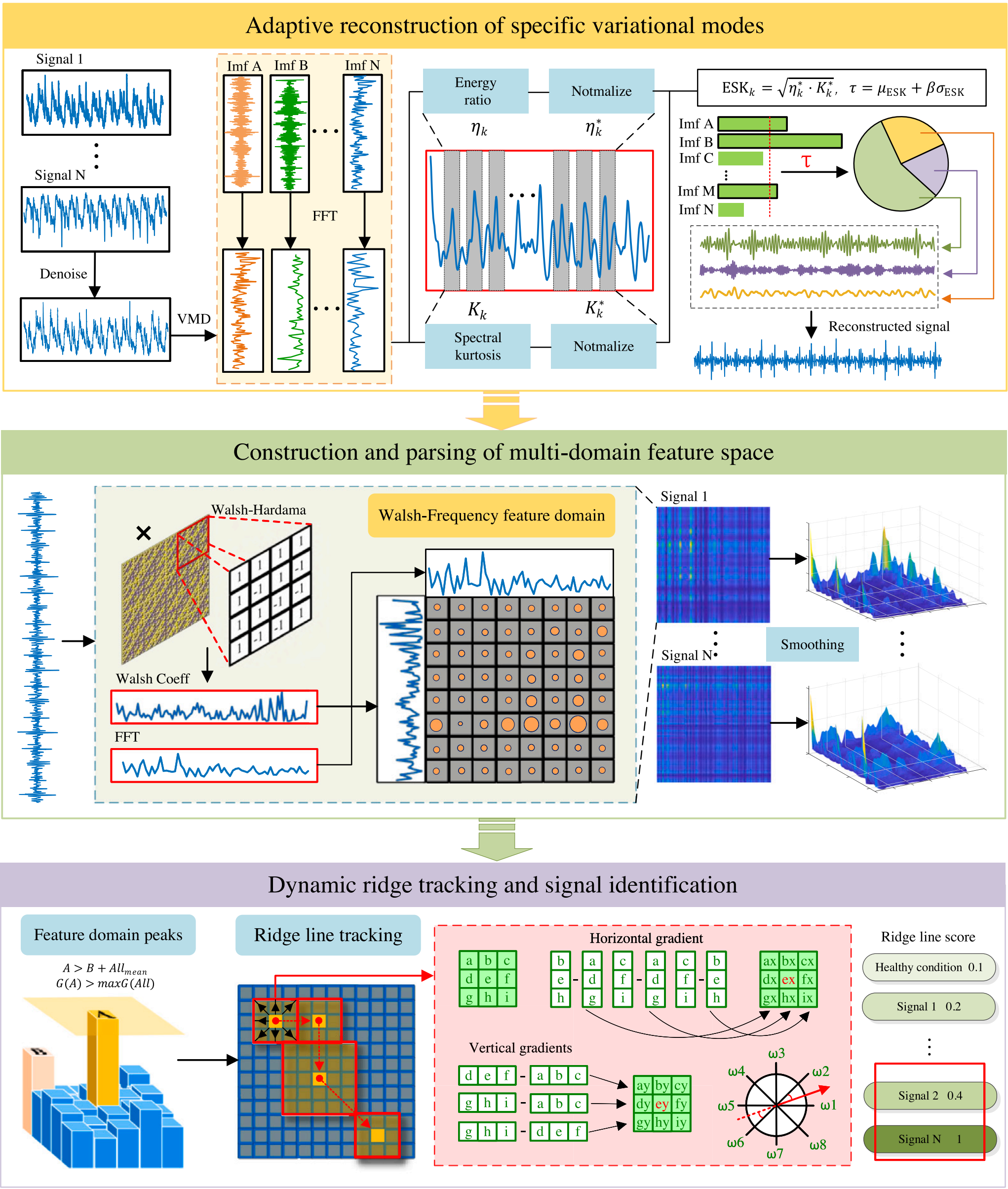

Fig. 1. The proposed framework for homotypic multi-source joint representation with dynamic hierarchical feature tracing in hybrid Walsh–frequency domain.

transform. $\mathrm{rect}(\cdot)$ is a rectangular window function, which only retains the spectral components in the frequency band centered at f_b. $\mathcal{F}^{-1}(\cdot)$ is the inverse Fourier transform, and $\mathbb{E}(\cdot)$ denotes the mathematical expectation operator. μ_k^b refers to the average value of the filtered signal, which is used for centralized processing. The kurtosis is used to evaluate the vibration impact degree of different IMF, which is complementary to the energy ratio and provides the corresponding weight. Specifically, this screening index directly locates the frequency bands most relevant to periodic impacts, effectively extracting target features while minimizing the interference of background noise and irrelevant components in multi-cylinder drilling pumps.

There are significant differences between the energy ratio and spectral kurtosis in dimension and numerical range($\eta_k \in [0,1]$, $\kappa_k \in \mathbb{R}$), which will lead to the problem of large number dominance and lose the balance of the two indicators. To synergize these complementary features, we construct the composite indicator ESK through a multi-stage normalization and fusion process. This ensures that neither the dimensionally distinct energy ratio nor the spectral kurtosis disproportionately dominates the selection criteria:

$$\eta_k^* = \frac{\eta_k - \min(\eta)}{\max(\eta) - \min(\eta) + \epsilon} \tag{10}$$

$$\kappa'_k = \operatorname{sgn}(\kappa_k) \cdot \ln(1 + |\kappa_k|) \tag{11}$$

$$\kappa^*_k = \frac{\kappa'_k - \min(\kappa')}{\max(\kappa') - \min(\kappa') + \epsilon} \tag{12}$$

$$\mathrm{ESK}_k = \sqrt{\eta^*_k \cdot \kappa^*_k} \tag{13}$$

where ϵ denotes the anti-division-by-zero constant (Set to 10^{-6}). The logarithmic transformation suppresses extreme kurtosis outliers, while the geometric mean $\sqrt{\eta^*_k \cdot \kappa^*_k}$ enforces a "mutual confirmation" logic: the final score is high only if a component exhibits both significant periodicity (Energy) and impulsiveness (Kurtosis).

Consequently, it is imperative to achieve adaptive matching of the signal characteristics pertinent to the current operating condition. To this end, an adaptive filtering threshold τ, formulated based on the data's statistical properties, is defined as follows:

$$\tau = \mu_{\mathrm{ESK}} + \beta\sigma_{\mathrm{ESK}}, \quad \mu_{\mathrm{ESK}} = \frac{1}{K}\sum_{k=1}^{K} \mathrm{ESK}_k, \quad \sigma_{\mathrm{ESK}} = \sqrt{\frac{1}{K}\sum_{k=1}^{K}(\mathrm{ESK}_k - \mu_{\mathrm{ESK}})^2} \tag{14}$$

where β denotes the adjustment coefficient, governing the stringency of the threshold. Its value corresponds to the multiple of the standard deviation and satisfies the relation $P(\mathrm{ESK}_k > \mu_{\mathrm{ESK}} + \beta\sigma_{\mathrm{ESK}}) \approx 1 - \Phi(\beta)$, where $\Phi(\cdot)$ is the standard normal distribution function. This design dynamically adapts the screening criteria according to the data distribution characteristics of the signal under the current operating condition, thereby enhancing the algorithm's adaptability to data from different load conditions. By tuning the multiple of the standard deviation, an effective balance is struck between sensitivity to fault signatures and robustness against noise. This provides an objective standard for IMF screening.

To ensure that salient fault signatures are preserved while maintaining screening efficiency, a dual-constraint selection mechanism is introduced. This mechanism integrates threshold-based screening with a minimum retained components guarantee, thereby achieving an optimal selection of IMF components. The selection logic is defined as follows:

$$\mathcal{K}_s = \left(\left\{k \mid \mathrm{ESK}_k > \tau\right\} \cup \mathrm{top}_M(\mathrm{ESK}_k)\right) \cap \left\{k \mid \mathrm{rank}(\mathrm{ESK}_k) \le N_{\max}\right\} \tag{15}$$

where M and $N_{\max}$ denote the upper limit on the number of IMF components with the highest comprehensive index and the lower limit on the minimum number of components to be retained, respectively. The intersection with $\mathrm{rank}(\mathrm{ESK}_k) \le N_{\max}$ acts as a "hard limiter" to prevent over-reconstruction, effectively filtering out lower-ranked components that are likely noise artifacts.

Subsequently, an inverse Softmax weighting strategy is implemented, strategically reducing contribution weights of high comprehensive indicator IMF components while amplifying weights of medium indicator components. The weighting coefficients w_k for each IMF are determined by:

$$w_k = \frac{\exp(\mathrm{ESK}_{\max} - \mathrm{ESK}_k)}{\sum_{i\in\mathcal{K}_s} \exp(\mathrm{ESK}_{\max} - \mathrm{ESK}_i)} \tag{16}$$

This weight-reversal mechanism achieves effective suppression of baseline vibration interference and directional enhancement of latent fault signatures through redistributing signal energy to selectively strengthen medium-saliency features with diagnostic significance. The signal reconstruction is then performed using the following formulation:

$$x_{\mathrm{recon}}(t) = \sum_{k\in\mathcal{K}_s} w_k \cdot u_k(t) \tag{17}$$

This section presents a novel adaptive variational mode reconstruction methodology that fundamentally transforms the approach to vibration detection in reciprocating machinery. The proposed method effectively addresses the traditional limitations of preset decomposition mode numbers in conventional VMD applications through harmonic band kurtosis and energy-based modal selection algorithms. By implementing automated identification and reconstruction of diagnostically significant vibration components, this approach circumvents the subjectivity inherent in traditional parameter-dependent methods. The integration of natural stroke frequency characteristics with adaptive statistical threshold processing enables superior noise immunity and consistent feature extraction across diverse pressure regimes without requiring manual intervention.

3.2. Construction and parsing of multi-domain feature space

The initial phase of feature extraction employs the Discrete Fourier Transform (DFT) to transform the reconstructed signal $x_{\mathrm{recon}}[n]$ from its temporal representation to the frequency domain. To analyze the frequency distribution of the reconstructed signal x_{recon}, we compute its single-sided amplitude spectrum $P[m]$. This transformation maps the time-domain series into spectral components, revealing the energy distribution across the discrete frequency bins:

$$X[m] = \sum_{n=0}^{N-1} x_{\mathrm{recon}}[n]e^{-\mathrm{j}\frac{2\pi}{N}mn}, \quad P[m] = \frac{2}{N}|X[m]| \quad (m = 0, 1, \dots, \lfloor N/2 \rfloor). \tag{18}$$

where N represents the total number of signal sampling points, $X[m]$ denotes the complex-valued spectrum, j is the imaginary unit, and $P[m]$ corresponds to the single-sided amplitude spectrum. This spectral representation provides crucial insights into the energy distribution across frequency components, enabling the identification of characteristic frequencies associated with reciprocating impact vibrations and their harmonic components.

Recognizing the limitations of purely frequency-domain analysis in distinguishing operational states of homotypic multi-source signals, the Walsh–Hadamard transform is introduced as a complementary analytical tool. Unlike Fourier analysis, which decomposes signals into smooth sinusoids, the Walsh–Hadamard transform utilizes a basis of orthogonal rectangular waveforms. This non-sinusoidal basis is defined by the kernel function $\mathrm{wal}(p,n)$, which toggles between +1 and −1 based on binary bit interactions, making it exceptionally sensitive to the sharp discontinuities and abrupt edges found in mechanical impact signals:

$$\mathrm{wal}(p,n)=\prod_{i=0}^{k-1}(-1)^{b_i(n)\cdot b_{k-1-i}(p)},\quad k=\log_2 N \tag{19}$$

where $b_i(n)$ denotes the ith bit of the binary representation of the ordinal number n. The Walsh transform coefficient $W[p]$ is computed through correlations between the input signal and Walsh basis functions, which are composed of rectangular waveforms taking only values of +1 and −1. This binary nature makes Walsh transforms particularly efficient for digital implementation, as the core operations reduce to XOR gates in hardware. Unlike the sinusoidal basis functions of Fourier analysis, Walsh functions excel at characterizing signal discontinuities and abrupt transitions, providing effective characterization for non-smooth signal discontinuities. The discrete Walsh transform coefficients are calculated as:

$$W[p]=\frac{1}{N}\sum_{n=0}^{N-1}x[n]\cdot\mathrm{wal}(p,n) \tag{20}$$

The preference for this rectangular basis is mathematically grounded in its ability to avoid the Gibbs phenomenon, a critical limitation in Fourier analysis where approximating step-like discontinuities results in persistent oscillation errors:

$$\lim_{N\to\infty}\left|f(t)-S_N^{\mathrm{Fourier}}(t)\right|_{\max}=\left(\frac{1}{\pi}\int_0^{\pi}\frac{\sin\tau}{\tau}d\tau-\frac{1}{2}\right)\cdot|\mathrm{jump}| \tag{21}$$

Conversely, the Walsh basis is defined by its Sequency (k), corresponding to the half-rate of zero-crossings, which allows it to track abrupt transitions without such artifacts:

$$k=\frac{1}{2}\lim_{T\to\infty}\frac{Z_c(T)}{T} \tag{22}$$

This linear relationship ensures that dense impact sequences are mapped to sparse, high-energy coefficients. As validated in hydraulic machinery applications, this property enables the effective isolation of fault features from heavy background noise [32] and facilitates the precise quantification of cyclostationary impulses [33], overcoming the limitations of traditional spectral leakage.

When transient impacts occur in vibration signals, their waveforms exhibit stronger correlations with certain rectangular Walsh basis functions, resulting in prominent peaks at corresponding sequency-domain positions. To ensure commensurability between the sequency and frequency domains prior to fusion, we apply a global normalization based on the infinity norm:

$$\bar{W}[p]=\frac{|W[p]|}{\|W\|_\infty+\epsilon},\quad \bar{P}[m]=\frac{P[m]}{\|P\|_\infty+\epsilon} \tag{23}$$

where $\|\cdot\|_\infty$ denotes the infinity norm of the signal, representing the maximum absolute value of all sample points.

The culmination of methodology introduces an innovative multi-domain fusion approach, establishing a highly discriminative joint feature domain. By synthesizing the strengths of both domains, we construct a hybrid Walsh–frequency feature space $H(m,f,p)$. This joint representation modulates the Walsh coefficients with frequency-domain amplitude information and a Gaussian weighting function, effectively highlighting impulse-rich regions while suppressing background spectral leakage:

$$H(m,f,p)=\bar{P}[m]\cdot\bar{W}[p]\cdot\exp\left(-\frac{(f-f_0)^2}{2(cf_0)^2}\right) \tag{24}$$

where the Gaussian term acts as a “soft band-pass filter” centered at f_0, focusing the analysis on the physically relevant bandwidth associated with the pump’s stroke mechanics. This Gaussian weighting, where f_0 represents the center frequency and c controls the bandwidth, isolates relevant frequency components while suppressing noise. This complements the Walsh transform’s ability to detect signal discontinuities, offering a dual perspective valuable for identifying both periodic behavior and sudden transient faults.

Multi-domain feature fusion significantly enhances fault diagnosis by satisfying three conditions: synchronization of feature locations, magnitude alignment, and interference suppression. By exploiting the complementary strengths of Fourier frequency components and Walsh discontinuity detection, this method filters out artifacts and robustly identifies genuine fault signatures, which is especially effective for separating homotypic multi-source signals.

3.3. Dynamic ridge tracking and signal identification

The systematic quantitative analysis of spatial features for effective failure mode extraction begins with the establishment of a gradient field calculation model. To extract fault features from this hybrid domain, we treat the feature map as a topographic surface and employ a gradient-based ridge tracking algorithm. The local gradient vector field is first computed to identify the direction of steepest ascent, which guides the tracing of energy ridges associated with fault impulses:

$$g_x[x,y]=\frac{1}{C_w}\sum_{i=-r_w}^{r_w}i\cdot H[x+i,y],\quad g_y[x,y]=\frac{1}{C_w}\sum_{j=-r_w}^{r_w}j\cdot H[x,y+j] \tag{25}$$

The window parameters are adaptively determined based on local signal characteristics:

$$r_w = \frac{w-1}{2}, \quad w = \begin{cases} 5, & \sigma_H > \tau_\sigma \cdot \max(H) \\ 3, & \sigma_H \le \tau_\sigma \cdot \max(H), \end{cases} \quad C_w = r_w(r_w+1) \tag{26}$$

Here, r_w denotes a square neighborhood window with a radius of $(w-1)/2$, while σ_H represents the local standard deviation within this defined region. Furthermore, τ_σ functions as the scalar peak coefficient, and $\max(H)$ corresponds to the maximum value observed within the window. The window size r_w balances gradient smoothness with feature preservation, while the normalization coefficient C_w ensures scale invariance across varying amplitudes.

Using these gradients, the direction angle is determined and a directional quantization model is established for the analysis of feature propagation. This relationship is formally expressed as:

$$\theta[x,y] = \operatorname{arctan2}(g_y[x,y], g_x[x,y]) \in [0, 2\pi), \quad \theta_d = \frac{2\pi(d-1)}{D}\,(d = 1, \dots, D) \tag{27}$$

where, $D = 4(w-1)$ represents the directional resolution, which exhibits dynamic adaptation based on the window dimensions. Fundamentally, this directional quantization system establishes a robust mapping relationship that bridges the continuous gradient field to the discrete directional template.

A directional weight function is then introduced to evaluate template matching and characterize the anisotropic response distribution. The mathematical formulation proceeds as follows:

$$w_d[x,y] = \exp\left(-\frac{(\theta[x,y]-\theta_d)^2}{2(\pi/D)^2}\right) \cdot \left(1 + \frac{H[x,y]}{\max(H)}\right) \tag{28}$$

$$\hat{w}_d[x,y] = \frac{w_d[x,y]}{\sum_{i=1}^{D} w_i[x,y]} \tag{29}$$

This formulation encompasses two essential components. The first component implements a direction similarity measure based on a Gaussian kernel, effectively quantifying the correlation between the current gradient direction and the template direction. The second component introduces adaptive weighting of feature strength, ensuring that regions exhibiting high response receive proportionally greater weight in the directional evaluation process. Normalization maintains weight comparability across all directions while directly reflecting the primary direction of feature propagation.

To improve robustness, a weighted evaluation framework for directional pairs is employed, with complementary 180°-opposed orientations incorporated to capture bidirectional peak propagation. Following this principle, the valid directional pair set within a single analysis window is rigorously established through the following formulation:

$$w_{\text{pair}}[d,d'] = \max(\hat{w}_d[x,y], \hat{w}_{d'}[x,y]), \quad d' = (d + \frac{D}{2}) \pmod{D} \tag{30}$$

Then, the valid directional pair set within a single analysis window can be deterministically established as follows:

$$\mathcal{D}_{\text{valid}} = \left\{(d,d') \mid w_{\text{pair}}[d,d'] \ge \frac{1}{D}\right\} \tag{31}$$

where the threshold $1/D$ establishes a crucial minimum weighting criterion that is equivalent to the average weight level. This threshold effectively filters out insignificant directional pairs that might otherwise introduce undesirable noise interference into the analysis.

Within the valid pairs, the principal tracking direction is determined to guide the ridge along the maximum energy path, with the optimal direction selected based on geometric continuity when weights are comparable, which are specified as:

$$(d^*, d'^*) = \arg \max_{(d,d') \in \mathcal{D}_{\text{valid}}} w_{\text{pair}}[d,d'] \tag{32}$$

$$\Delta s[x,y] = r_w \cdot \left\lceil s_0 + \lambda \cdot \frac{H[x,y]}{\max(H)} \right\rceil \tag{33}$$

where s_0 represents the base step length, while λ governs the degree of strength adaptation. The ridge tracking step length implements an adaptive mechanism that effectively balances both the base step length and local feature response intensity. This adaptive approach allows for larger steps in regions characterized by strong feature responses, thereby improving computational efficiency, while employing smaller steps in weak response regions to maintain precise tracking accuracy.

The ridge line tracking process initiates from carefully selected salient feature points, where local maxima in the heatmap correspond to high-energy regions and serve as optimal starting points. The selection process implements a rigorous dual-criteria system, formalized as:

$$\left(x_{t+1}, y_{t+1}\right) = \left(x_t, y_t\right) + \Delta s[x_t, y_t] \cdot \left(\cos\theta_{d^*}, \sin\theta_{d^*}\right) \tag{34}$$

$$\mathcal{P} = \left\{ (x_0^*, y_0^*) \;\middle|\; \begin{array}{l} H[i,j] = \max_{(x,y)\in\mathcal{W}_{i,j}} H[x,y], \\ H[i,j] > H_{\text{second}}^{(i,j)} + \frac{H[i,j]-\mu_W^{(i,j)}}{2} \end{array} \right\} \tag{35}$$

In this formulation, $\mathcal{W}_{i,j}$ represents the local window centered at coordinates (i,j), $H_{\text{second}}^{(i,j)}$ denotes the second-largest value within the window, and $\mu_W^{(i,j)}$ represents the mean-shift term. The first criterion ensures that the initial point constitutes a local maximum, while the second criterion serves to exclude spurious peaks through evaluation of their relative difference to the subdominant value. Although this stringent initialization strategy may reduce the number of eligible starting points, it significantly enhances tracking reliability by ensuring robust ridge origins.

The ridge line is constructed by sequentially recording spatial coordinates, using termination conditions to prevent infinite iteration. The termination criteria are comprehensively defined as:

$$\mathcal{R} = \left\{ \left(x_t, y_t \right) \right\}_{t=0}^{T}, \quad (x_0, y_0) \in \mathcal{P}, \quad \mathcal{R}_{t+1} = \mathcal{R}_t \cup \left\{ \left(x_{t+1}, y_{t+1} \right) \right\} \tag{36}$$

$$T = \min \left\{ t \,\middle|\, \begin{array}{c} H[x_t, y_t] < \tau_{\text{term}} \cdot \max(H), \\ (x_t, y_t) \notin [1, M] \times [1, N], \\ \sum\limits_{(d,d') \in \mathcal{D}_{\text{valid}}} w_{\text{pair}}^2 < \gamma_{\text{term}} \end{array} \right\} \tag{37}$$

Within this framework, τ_{term} denotes the termination coefficient, while γ_{term} represents the threshold for the squared sum of directional pair weights. The tracking process terminates under three specific conditions: feature disappearance when signal strength becomes undetectable, boundary violation upon exceeding valid spatial domains, and directional ambiguity occurring when no dominant propagation path can be identified from the weight distribution.

Finally, we define a quantitative fault indicator $\mathcal{F}_{\text{prl}}$ by aggregating the topological properties of the extracted ridges. This model integrates the number of ridges M (complexity), their continuity μ_L (persistence), and their intensity μ_I (energy), normalized by the domain size $|\mathcal{H}|$ to ensure robustness against signal scaling:

$$\mathcal{F}_{\text{prl}} = \frac{M \cdot \mu_L \cdot \left(1 + \frac{\sigma_L}{\mu_L}\right) \cdot \mu_I}{|\mathcal{H}|}, \quad M = |\{\mathcal{R}_k\}|, \quad \mu_L = \text{mean}(|\mathcal{R}_k|), \quad \mu_I = \frac{1}{M} \sum_{k=1}^{M} \max_{(x,y) \in \mathcal{R}_k} \mathcal{H}(x, y) \tag{38}$$

In this comprehensive model, M represents the number of detected ridges, effectively capturing the distribution density of vibration characteristics and revealing subtle differences between various signals. The parameter μ_L quantifies the average ridge length, thereby measuring the continuous diffusion capability of the main vibration energy propagation. The term $1 + \frac{\sigma_L}{\mu_L}$ functions as a variation coefficient gain term, where the generation of fractured ridges during tracking interruption directly influences the standard deviation σ_L, amplifying structural instability indicators. Furthermore, μ_I represents the peak energy density along the ridge path, amplifying the differential intensity ratio supported by dynamic evolution characteristics between different signals. Finally, $\mathcal{H}$ denotes the size of the feature domain, which, after appropriate normalization, enables robust diagnostic separation in multi-source signals of similar types.

Building upon the theoretical framework established above, we present Algorithm 1, which delineates the systematic implementation of our proposed homotypic multi-source joint representation methodology. This novel approach integrates dynamic hierarchical feature tracing within the hybrid Walsh–frequency domain, enabling robust feature extraction and enhanced signal processing capabilities while maintaining computational efficiency through optimized matrix operations.

4. Experimental validation and analysis

This section presents a comprehensive validation of our proposed methodology, beginning with a detailed description of the apparatus configuration and dataset description in Section 4.1. Subsequently, Section 4.2 offers a thorough experimental validation through four distinct case studies, where we systematically evaluate the efficacy and performance metrics of our proposed methods in comparison with established approaches in the field.

4.1. Experimental apparatus configuration and dataset description

The experimental investigation utilized a drilling pump set platform incorporating a comprehensive data acquisition system for real-time signal monitoring. As detailed in the revised Fig. 2, specifically in panel (d) Sensors array installation, the monitoring configuration consists of a hybrid sensor array mounted on each cylinder. This array comprises piezoelectric accelerometers to capture high-frequency vibration signatures and strain sensors strategically positioned to monitor stress distribution and structural deformation. The experimental dataset encompassed measurements from components returned from active drilling sites, ensuring authentic operational conditions. Although the full experimental database covers a wide operational spectrum including 50, 90, 110, and 130 Strokes Per Minute (SPM), the current analysis specifically focuses on the 50 SPM condition with corresponding pressure variations ranging from 10 to 40 MPa per stroke setting. This selection aims to validate the method's sensitivity under low-speed regimes where fault features are inherently weaker. The research systematically examined multiple degradation scenarios, progressing from baseline health states through early-stage wear patterns, intermediate deterioration states, to severe structural degradation in both suction and discharge valves, as visually depicted in Fig. 3. In healthy states, valve components maintained structural integrity, while progressive deterioration manifested as increasingly severe cracking patterns in both the valve body and metal components. Data acquisition for both the acceleration and strain channels was conducted at a 1 kHz sampling frequency (1 ms

Algorithm 1 The proposed homotypic multi-source joint representation with dynamic hierarchical feature tracing in hybrid Walsh–frequency domain

```
Phase I: A statistical-energy approach for complex mechanical systems
Input: Raw vibration signal $x(t)$, stroke period $T_s$
Define $\Omega_{\text{stroke}} \leftarrow \{f_0, 2f_0, \dots, n_{\max} f_0\},\ f_0 = 1/T_s$    ▷ Eq. (7)
$\{u_k(t)\} \leftarrow \text{VMD}(x(t))$
for $k = 1$ to $K$ do
    $\eta_k \leftarrow \frac{\sum_b \int_{\Delta f} |\hat{u}_k|^2}{\int_0^\infty |\hat{u}_k|^2},\ \kappa_k \leftarrow \max_b \left( \frac{E[(u_k^b - \mu_k^b)^4]}{(E[(u_k^b - \mu_k^b)^2])^2} - 3 \right)$    ▷ Eq. (8), (9)
    $\eta_k^* \leftarrow \frac{\eta_k - \min \eta}{\max \eta - \min \eta + \epsilon},\ \kappa_k' \leftarrow \text{sign}(\kappa_k) \ln(1 + |\kappa_k|),\ \kappa_k^* \leftarrow \frac{\kappa_k' - \min \kappa'}{\max \kappa' - \min \kappa' + \epsilon}$    ▷ Eq. (10)-(12)
    $\text{ESK}_k \leftarrow \sqrt{\eta_k^* \cdot \kappa_k^*}$    ▷ Eq. (13)
end for
Output: $\{\text{ESK}_k\}_{k=1}^K$
Phase II: Construction and parsing of multi-domain feature space
Input: ESK indicators $\{\text{ESK}_k\}_{k=1}^K$
$\mu_{\text{ESK}} \leftarrow \frac{1}{K} \sum \text{ESK}_k,\ \sigma_{\text{ESK}} \leftarrow \sqrt{\frac{1}{K} \sum (\text{ESK}_k - \mu_{\text{ESK}})^2},\ \tau \leftarrow \mu_{\text{ESK}} + \beta \sigma_{\text{ESK}}$    ▷ Eq. (14)
$\mathcal{K}_s \leftarrow (\{k \mid \text{ESK}_k > \tau\} \cup \text{top}_M(\text{ESK})) \cap \{k \mid \text{rank}(\text{ESK}_k) \le N_{\max}\}$    ▷ Eq. (15)
$w_k \leftarrow \frac{\exp(\max_{\mathcal{K}_s} \text{ESK} - \text{ESK}_k)}{\sum_{\mathcal{K}_s} \exp(\max_{\mathcal{K}_s} \text{ESK} - \text{ESK}_i)}$    ▷ Eq. (16)
$x_{\text{recon}} \leftarrow \sum_{\mathcal{K}_s} w_k u_k$    ▷ Eq. (17)
$X[m] \leftarrow \sum_{n=0}^{N-1} x_{\text{recon}} e^{-j2\pi mn/N},\ P[m] \leftarrow \frac{2}{N} |X[m]|$    ▷ Eq. (18)
$W[p] \leftarrow \frac{1}{N} \sum_{n=0}^{N-1} x_{\text{recon}} \cdot wal(p, n),\ \bar{P}[m] \leftarrow \frac{P[m]}{\|P\|_\infty + \epsilon},\ \bar{W}[p] \leftarrow \frac{|W[p]|}{\|W\|_\infty + \epsilon}$    ▷ Eq. (20), (23)
$H(m, p) \leftarrow \bar{P}[m] \cdot \bar{W}[p] \cdot \exp\left( -\frac{(f - f_0)^2}{2(c f_0)^2} \right)$    ▷ Eq. (24)
Output: $H(m, p)$
Phase III: Dynamic ridge tracking and signal identification
Input: Feature domain $H$
$\mathcal{R} \leftarrow \emptyset,\ \mathcal{P} \leftarrow$ dual-criterion peaks    ▷ Eq. (35)
for each $(x_0, y_0) \in \mathcal{P}$ do
    $\mathcal{R}_k \leftarrow \{(x_0, y_0)\},\ t \leftarrow 0$
    while not terminated do    ▷ Eq. (37)
        $g_x, g_y \leftarrow$ adaptive gradient, $w \leftarrow$ window size    ▷ Eq. (25), (26)
        $\theta_d, \hat{w}_d \leftarrow$ direction angles and weights    ▷ Eq. (27), (28)
        $(d^*, d'^*) \leftarrow \arg\max \hat{w}_d,\ \Delta s \leftarrow r_w \lceil s_0 + \lambda H / \max H \rceil$    ▷ Eq. (32), (33)
        $(x_{t+1}, y_{t+1}) \leftarrow (x_t, y_t) + \Delta s (\cos \theta_{d^*}, \sin \theta_{d^*})$    ▷ Eq. (34)
        $\mathcal{R}_k \leftarrow \mathcal{R}_k \cup \{(x_{t+1}, y_{t+1})\},\ t \leftarrow t + 1$
    end while
    $\mathcal{R} \leftarrow \mathcal{R} \cup \{\mathcal{R}_k\}$
end for
$M \leftarrow |\mathcal{R}|,\ \mu_L \leftarrow$ mean length, $\sigma_L \leftarrow$ std length, $\mu_I \leftarrow$ mean max intensity
$F_{\text{prl}} \leftarrow \frac{M \cdot \mu_L \cdot (1 + \sigma_L / \mu_L) \cdot \mu_I}{|\mathcal{H}|}$    ▷ Eq. (38)
Output: $F_{\text{prl}}$
```

intervals). This sampling rate was selected to align with industry-standard operational parameters, where pump strokes typically range from 70—120 SPM, with maximum operational limits of 120 SPM. Although the full experimental database covers a wide operational spectrum including 50, 90, 110, and 130 SPM, the current analysis specifically focuses on the 50 SPM condition across varying discharge pressures (10–40 MPa). It is crucial to emphasize that the 50 SPM condition was deliberately selected as the primary benchmark because it physically represents the most demanding diagnostic scenario. At this low speed, the mechanical impact energy generated by valve degradation is exceptionally weak, resulting in the lowest Signal-to-Noise Ratio (SNR) and the most severe homotypic aliasing interference. In contrast, higher rated speeds naturally produce more prominent and easily identifiable fault impulses. Therefore, achieving reliable feature extraction and spatial isolation under these extreme conditions provides a rigorous demonstration of the proposed framework's foundational robustness and its sensitivity to incipient faults.

4.2. Experimental validation and comparative analysis

4.2.1. Case study I

In a comprehensive experimental investigation conducted under strictly controlled conditions, vibration signals were systematically acquired from the first cylinder of a multi-cylinder hydraulic pump system, maintained at a steady operating pressure

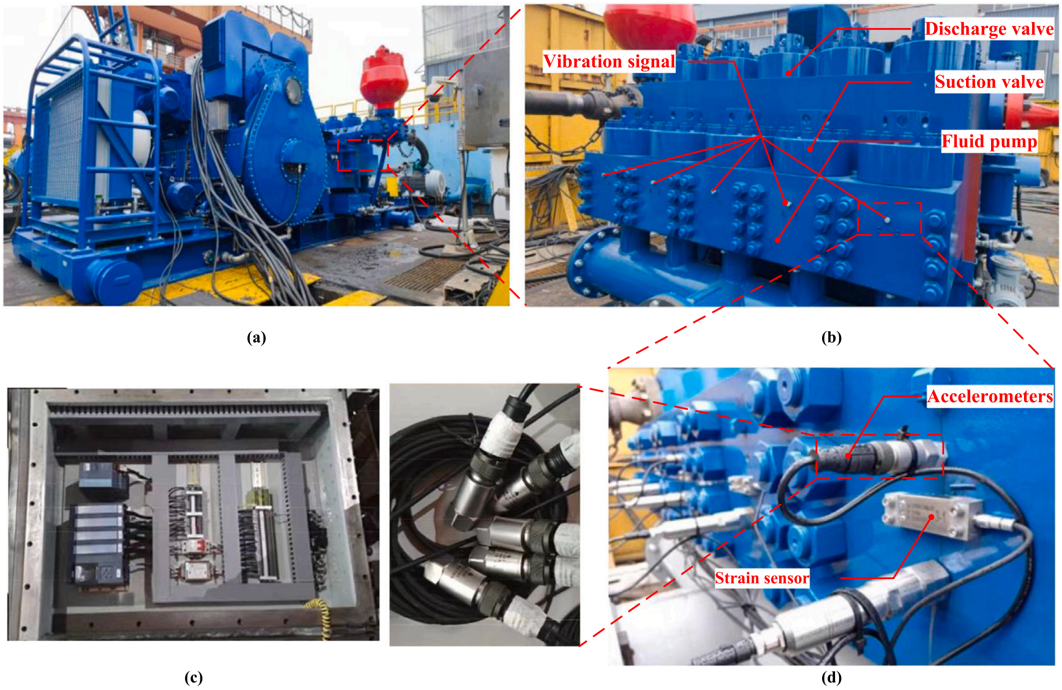

Fig. 2. Schematic representation of the experimental apparatus configuration: (a) Hydraulic pump assembly with multiple cylinders, (b) Fluid end chamber with integrated flow path connections, (c) Data collection and signal transmission system, (d) Sensors array installation.

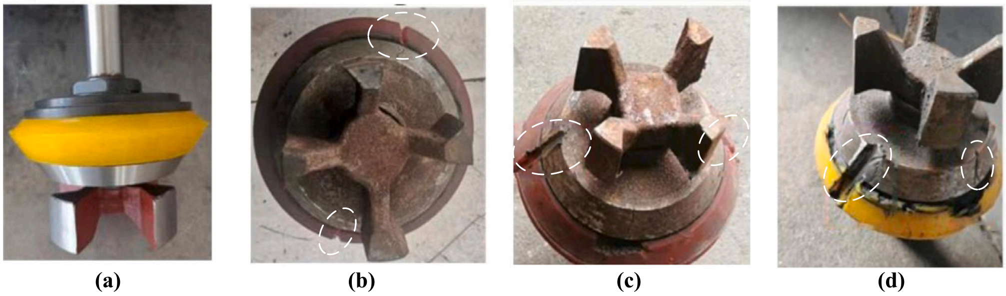

Fig. 3. Progressive deterioration stages of the valve body: (a) Health operational condition, (b) Early-stage wear pattern, (c) Intermediate deterioration state, (d) Severe structural degradation.

of 10 MPa throughout the testing protocol. The data acquisition process utilized an array of multi-channel sensors strategically positioned to capture the system's dynamic response. As evidenced in Fig. 4, when the system achieved steady-state operation with a stabilized impact period of 1.2 s (corresponding to a fundamental frequency of 0.83 Hz), the channel waveforms exhibited remarkable similarity across four distinct health states: suction valve fault, discharge valve fault, healthy condition, and dual valve fault. These waveforms demonstrated such profound visual indistinguishability that conventional observation methods proved insufficient for condition discrimination. Furthermore, the time-domain responses consistently manifested periodic oscillation patterns characterized by overlapping amplitude ranges and intricate phase features that defied straightforward interpretation. Despite the presence of inherent mechanical disparities among the various health states, critical diagnostic indicators—including but not limited to amplitude distributions, phase signatures, and localized extremum profiles—revealed no statistically significant variations that could serve as reliable fault indicators. Of particular significance is the observation that transient impact components were thoroughly masked by the complex interplay between coupled environmental noise and intrinsic system dynamics, thereby rendering conventional time-domain analysis methods ineffective for extracting fault-sensitive signatures.

Building upon these initial observations, Variational Mode Decomposition (VMD) was subsequently employed to process and analyze signals obtained from all four health states. Fig. 5 presents a detailed delineation of the time-domain waveforms corresponding to nine Intrinsic Mode Functions (IMFs) at 10 MPa, which revealed a characteristic hierarchical energy distribution pattern. Specifically, IMF1 through IMF3 exhibited predominantly high-frequency, noise-dominated stochastic fluctuations, wherein the suction valve fault waveform, as illustrated in Fig. 5(a), initially displayed distinctive amplitude escalation. However, this

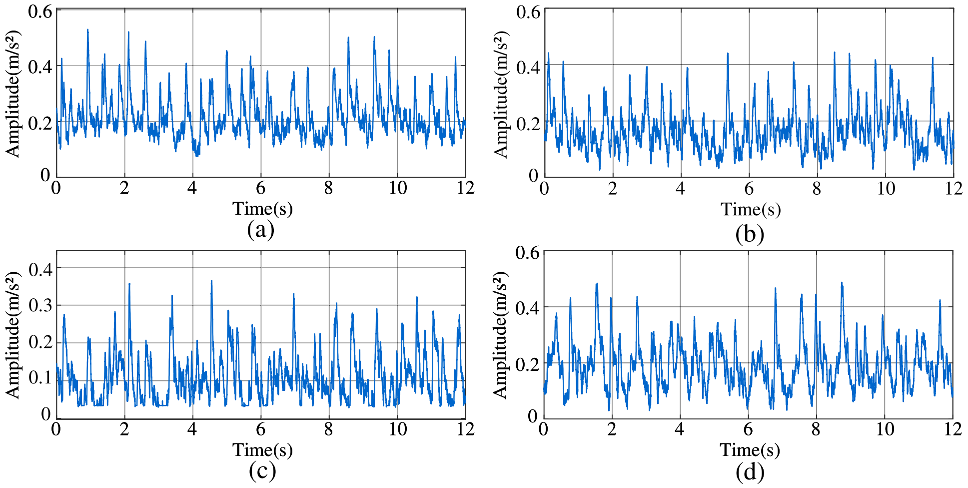

Fig. 4. Time-domain vibration signals from multiple sensor channels under 10 MPa working pressure: (a) Suction valve fault; (b) Discharge valve fault; (c) Healthy operation; and (d) Dual valve fault.

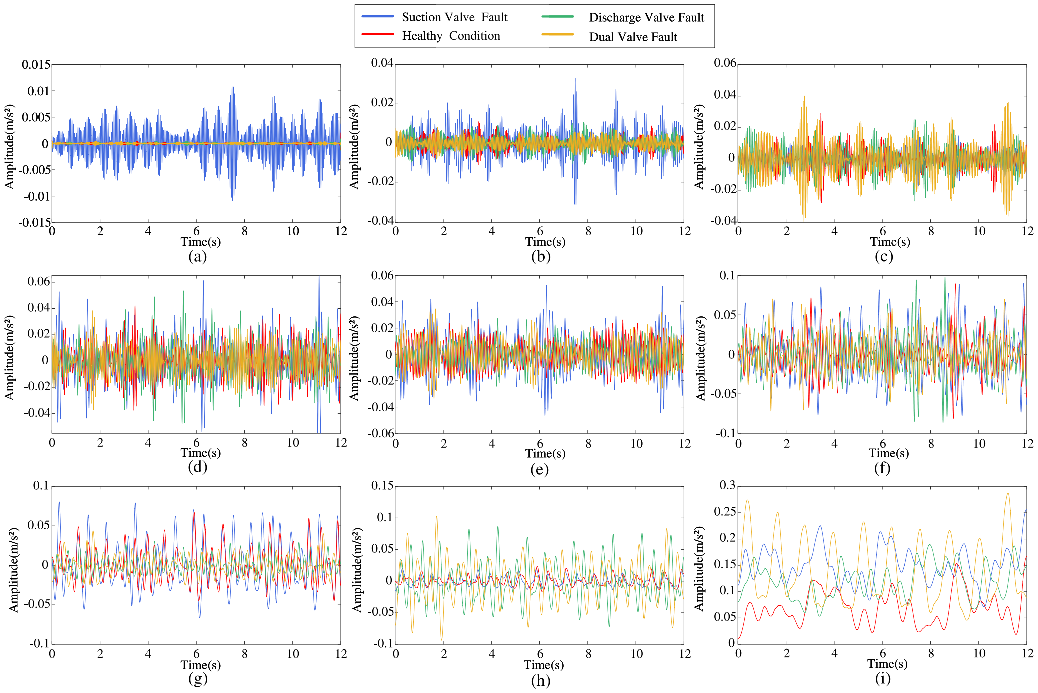

Fig. 5. Decomposed time-domain waveforms through VMD analysis at 10 MPa pressure: (a)–(i) IMF(1) through IMF(9).

distinguishing characteristic became increasingly obscured when examined in conjunction with other operational signatures, as demonstrated in Fig. 5(c). Conversely, IMF9 manifested primarily as low-frequency oscillations that showed strong correlation with system inertial characteristics, notably exhibiting substantially broader energy envelopes in comparison to their higher-frequency counterparts. Although IMF4 through IMF8 demonstrated clear associations with the hydraulic pump's fundamental stroke cycle (1.2s), detailed examination of Fig. 5(f) through Fig. 5(h) revealed extensive waveform synchronicity across all health states, with only sporadic and minimal localized amplitude separations while maintaining coherent oscillation structures throughout the analysis period.

Further investigation through spectral analysis, as presented in Fig. 6, revealed additional fundamental limitations in the diagnostic approach. Within the critical diagnostic frequency band of 0.5–10 Hz, persistent spectral band coalescence was observed across multiple components. A particularly noteworthy observation was the extensive interweaving of spectral peaks between discharge valve fault and healthy operation conditions in IMF5. Moreover, examination of IMF7 at the fundamental frequency

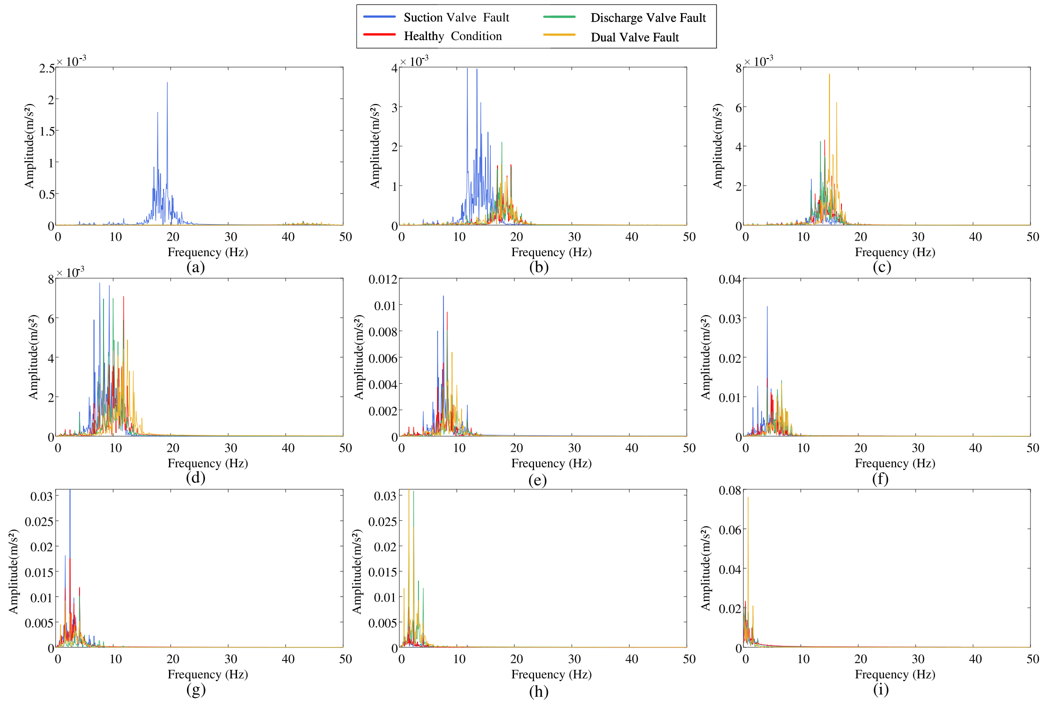

Fig. 6. Frequency-domain spectral analysis of VMD-processed signals at 10 MPa pressure: (a)–(i) IMF(1) through IMF(9).

(0.83 Hz) revealed an unexpected phenomenon wherein the dual valve fault condition demonstrated counterintuitive energy attenuation when compared to the baseline healthy operation. This simultaneous occurrence of stochastic temporal distinctions and paradoxical frequency-domain manifestations provides compelling evidence that visual characteristics extracted from individual components, when considered in isolation, cannot serve as reliable fault identification criteria.

The analytical characterization of decomposed signals was conducted through the framework delineated in Eq. (7) through Eq. (13). A comprehensive analysis of the energy ratio and spectral kurtosis distributions across Intrinsic Mode Functions (IMFs) under four distinct health states revealed several noteworthy patterns, as illustrated in Fig. 7. The initial seven IMFs (IMF1-IMF7) exhibited consistently high spectral kurtosis values with remarkably stable distribution patterns, while IMFs 6 through 9 demonstrated progressively increasing energy ratios, with IMF8 showing the most significant energy concentration. This pattern substantiates the theoretical foundation indicating that lower-frequency IMFs serve as primary carriers of fundamental impact frequencies. A particularly significant finding emerged in the analysis of IMF7, where healthy operational states displayed markedly reduced energy ratios compared to cases involving dual valve faults, as evidenced in Fig. 7(c) and Fig. 7(d). The spectral kurtosis distributions exhibited condition-specific signatures: discharge valve fault conditions (Fig. 7(b)) showed near-zero kurtosis baselines with sporadic peaks in isolated components, while both healthy and dual valve fault conditions maintained elevated spectral kurtosis values across lower-order IMFs, accompanied by a universal decay pattern in IMF8's kurtosis profile across all health states. These distinctive characteristics led to the development of an integrated selection protocol that optimally targets IMF components 6–7, effectively balancing energy concentration and transient impact representation across various operational scenarios.

Fig. 8 presents a comprehensive visualization of the weight distribution scheme derived through Eq. (16). The implemented inverse Softmax formulation strategically enhances contributions from medium ESK components in a systematic manner. Under suction valve fault conditions, as clearly observable in Fig. 8(a), IMF6 receives a relatively modest 35% weighting allocation despite its superior ESK metrics, while components exhibiting higher ESK values obtain proportionally amplified representation. This apparently counterintuitive weighting effect serves a deliberate purpose: it effectively suppresses background vibration interference emanating from high ESK components while simultaneously emphasizing diagnostically critical signals carried by medium ESK components, particularly IMF6. Consequently, the differential weight assignments within reconstructed signals effectively amplify subtle fault signatures while methodically eliminating the information loss typically inherent in single component selection methodologies.

Before proceeding to the final signal reconstruction, it is crucial to validate the algorithmic robustness. Therefore, regarding the parameter settings of VMD, we adopted the default values of mode number $K = 9$ and penalty factor $\alpha = 2000$. To conduct a parameter sensitivity test and verify that our framework does not depend on prior knowledge, we investigated the impacts of mode number and penalty factor on the signal-to-noise ratio (SNR) of the reconstructed signal over a wide range of values. Experiments were carried out using the suction valve fault data under the condition of 10 MPa. The results, as shown in Fig. 9, demonstrate extremely high stability of the proposed algorithm. Specifically, the SNR is relatively low only for the penalty factor of 1500 when

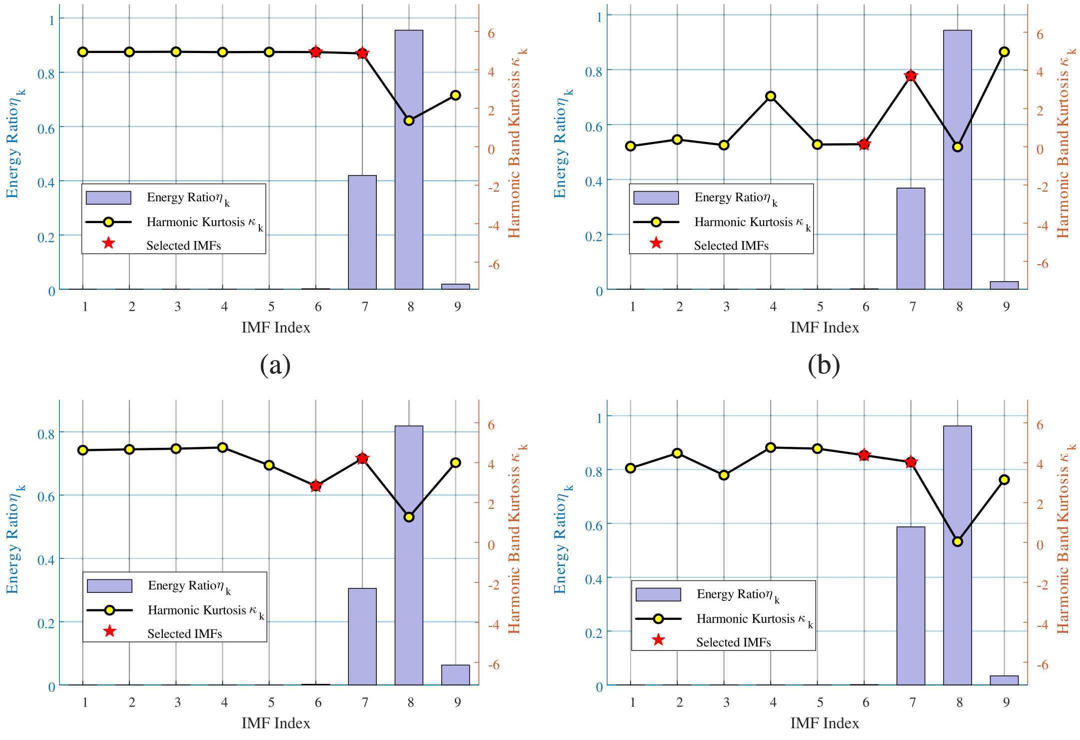

(a) (b)

(c) (d)

Fig. 7. IMF selection criteria analysis using energy ratio and kurtosis values: (a) Suction valve fault; (b) Discharge valve fault; (c) Healthy operation; (d) Dual valve fault.

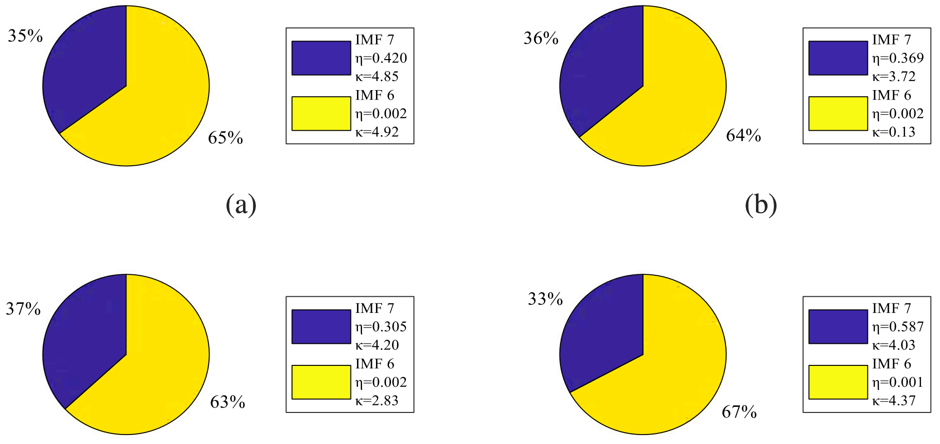

(a) (b)

(c) (d)

Fig. 8. Optimized weighting coefficients for IMF signal reconstruction: (a) Suction valve fault; (b) Discharge valve fault; (c) Healthy condition; (d) Dual valve fault.

$K = 6$. Once $K \geq 7$, the SNR rises rapidly and stabilizes, remaining nearly unchanged with the variation of K, and there is essentially no difference among the curves corresponding to different penalty factors. These findings indicate that our algorithm is robust against strong noise and can achieve reliable signal reconstruction without the need for elaborate parameter tuning.

The signal reconstruction process, executed through Eq. (17), yields remarkable improvements in both qualitative and quantitative aspects when compared to the original measurements, as depicted in Fig. 10. The reconstructed waveforms demonstrate superior preservation of critical impulsive characteristics while achieving substantial attenuation of high-frequency noise artifacts and

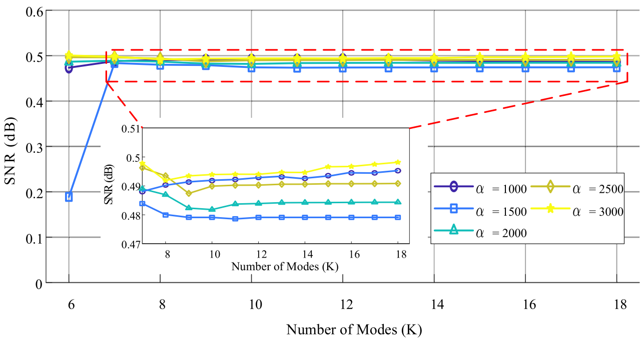

Fig. 9. Impact of mode number K and penalty factor α on the SNR of the reconstructed signal under 10 MPa.

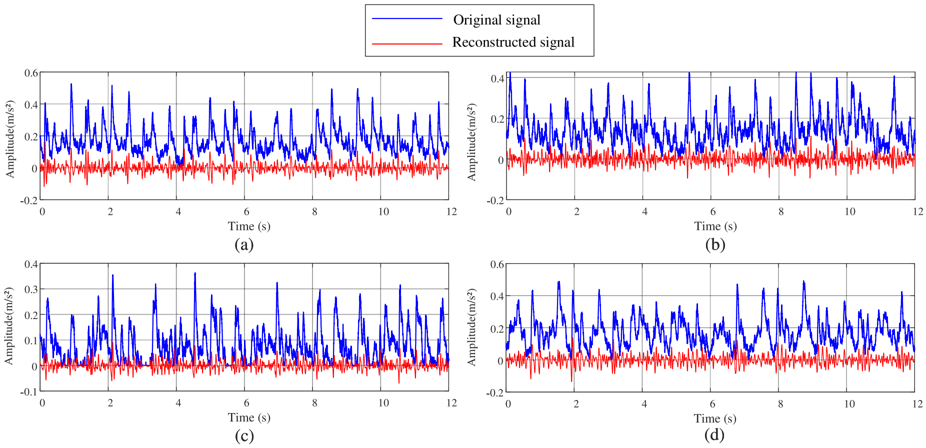

(a)

(b)

(c)

(d)

Fig. 10. Original versus reconstructed signals: (a) Suction valve fault (b) Discharge valve fault (c) Healthy condition (d) Dual valve fault.

baseline vibration fluctuations. This enhancement is facilitated by the inverse-Softmax weighting mechanism, which establishes an optimal balance between signal fidelity and noise suppression through selective amplification of diagnostically relevant components. The methodology's effectiveness is particularly evident in its ability to maintain the integrity of fault-indicative features while systematically reducing background interference that typically obscures the original signals.

Comprehensive spectral analysis, as presented in Fig. 11, further validates the advantages of the implemented reconstruction methodology. All operational states maintain consistent energy concentration at both fundamental and harmonic frequencies, while the healthy condition exhibits particularly distinctive spectral signatures characterized by amplitude attenuation and harmonic sparsification relative to fault conditions. This differential enhancement effectively amplifies the spectral divergence between healthy and faulty states, thereby establishing a more robust and discriminative basis for reliable condition identification in complex mechanical systems.

Building on these spectral insights, we further evaluate the comparative efficacy in the time domain. Specifically, Fig. 12 presents a detailed comparison of the fault extraction performance. As illustrated in Fig. 12(a), the signal reconstructed by the proposed method exhibits a significantly cleaner background compared to the other approaches. By adaptively screening for IMFs with high energy ratio and harmonic kurtosis, our method effectively filters out stochastic interference, recovering fault impulses with consistent periodicity. In contrast, Fig. 12(b) reveals that the Impulsive Mode Decomposition (IMD) [17] method exhibits evident waveform distortion and irregularity. Meanwhile, the waveforms generated by Maximum Correlated Kurtosis Deconvolution (MCKD) [29] in Fig. 12(c) and Multipoint Optimal Minimum Entropy Deconvolution Adjusted (MOMEDA) [34] in Fig. 12(d) display noticeable "glitches" and persistent high-frequency residue between impulse peaks, failing to fully suppress the background interference. Furthermore, the recently proposed MTSK-HMMS-S method (Fig. 12(e)) demonstrates commendable performance in achieving an exceptionally clean background, effectively zeroing out stochastic noise between impacts. However, it simultaneously exposes a critical drawback regarding amplitude consistency. Because the algorithm relies on a rigid time-shifting mechanism based on a fixed prior pump cycle, it struggles to accommodate natural mechanical phase variations. Consequently, certain valid impact peaks are artificially attenuated, resulting in the loss of the true physical energy envelope of the fault.

Complementing the qualitative visual assessment, we quantitatively validated the reconstruction quality by constructing a comprehensive evaluation system spanning the time and frequency domains using four metrics: Envelope Signal-to-Noise Ratio (ESNR) [35], Noise Reduction Ratio (NRR) [36], Spectral Entropy (SE) [37], and Multiscale Fuzzy Entropy (MFE) [38]. ESNR

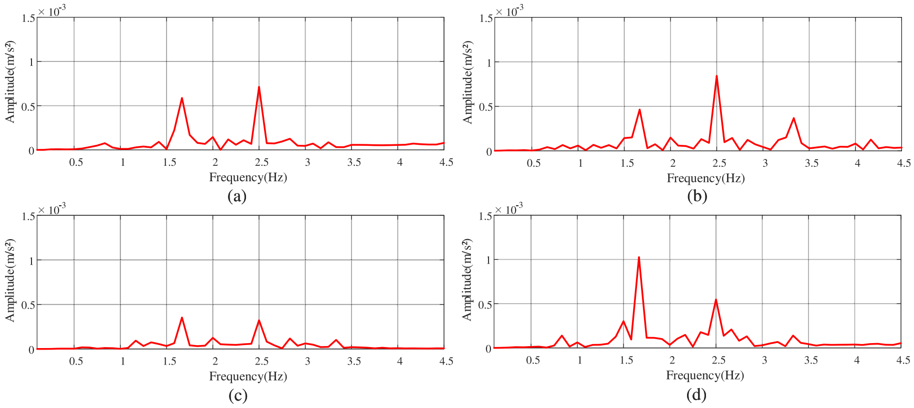

Fig. 11. Spectral analysis of reconstructed signals at 10 MPa: (a) Suction valve fault (b) Discharge valve fault (c) Healthy condition (d) Dual valve fault.

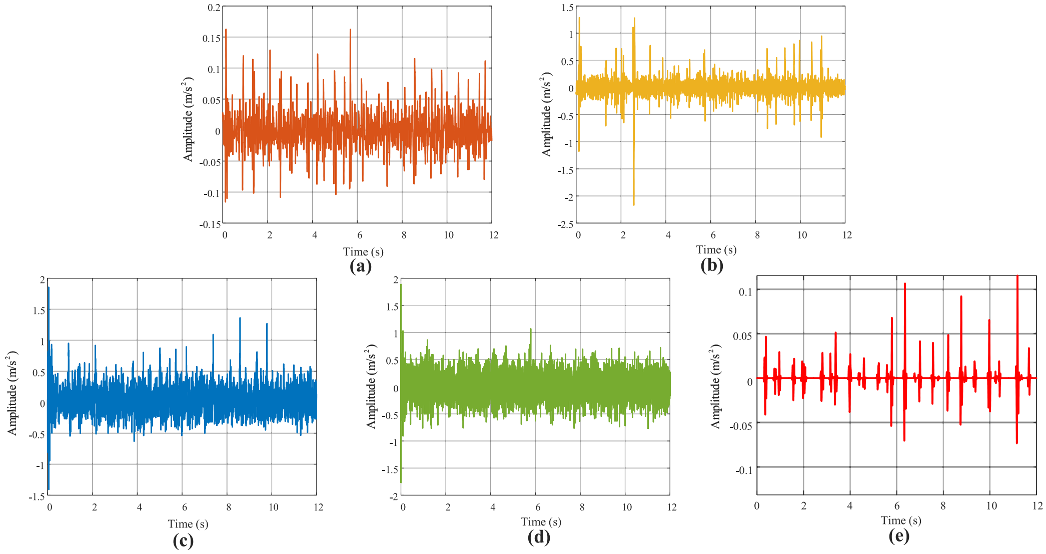

Fig. 12. Comparison of reconstructed time-domain signals at 10 MPa: (a) The proposed method (b) IMD (c) MCKD (d) MOMEDA (e) MTSK-HMMS-S.

quantifies the prominence of fault characteristic harmonics in the envelope spectrum; a higher value indicates stronger periodic impulse extraction. NRR measures the energy purification relative to the raw signal, serving as a direct indicator of noise elimination efficiency. Conversely, SE and MFE are negative indicators: lower Spectral Entropy implies a more concentrated energy distribution around fault frequencies, while lower Multiscale Fuzzy Entropy indicates higher signal regularity and reduced stochastic complexity. As detailed in Table 1, while traditional deconvolution methods (MCKD, MOMEDA) yield negative NRR values due to high-frequency noise amplification, the MTSK-HMMS-S method achieves exceptionally high NRR (90.86%) and low MFE (0.0374). This quantitatively corroborates its visual strength in forcibly zeroing out background noise. However, this extreme numerical purity is achieved through rigid time-domain truncation, which, as analyzed previously, compromises the physical amplitude envelope. In contrast, the proposed method (NRR=86.43%, ESNR=−0.1939 dB) maintains a physically balanced reconstruction, effectively suppressing stochastic interference without sacrificing the structural fidelity of the periodic impacts.

Upon establishing the feature domain, the two-dimensional planar feature domain heatmap, as illustrated in Fig. 13, demonstrates notable sparse characteristics, wherein the signal energy manifests in discrete concentrations across the two-dimensional plane, while the majority of the matrix regions exhibit negligible energy values approaching zero. Although preliminary distinctions have been observed among various health states—specifically manifesting as clustered energy concentrations at particular frequency coordinates for suction valve faults, multiple dispersed cluster formations for bilateral faults, and diffuse distribution patterns for both healthy states and discharge valve faults—these discriminative features lack robust quantitative characterization due to the compounded effects of background noise interference and fragmented energy distribution patterns. Consequently, this presents

Table 1
Quantitative comparison of signal reconstruction performance across different pressure conditions using ESNR, NRR, SE, and MFE.

Condition	Method	ESNR (dB)	NRR (%)	SE	MFE
10 MPa	Proposed Method	**−0.1939**	**86.43**	**4.8524**	**0.2298**
	IMD	−3.1435	−388.22	5.9605	0.6990
	MCKD	−6.7374	−362.30	7.2436	1.3515
	MOMEDA	−13.4740	−388.37	8.3709	1.2983
	MTSK-HMMS-S	2.0000	90.86	4.4801	0.0374
20 MPa	Proposed Method	**0.9773**	**90.60**	**4.5610**	**0.1402**
	IMD	0.8753	−238.44	5.0271	0.3434
	MCKD	−3.5199	−216.60	5.4821	0.6925
	MOMEDA	−9.6201	−238.51	8.2739	1.0259
	MTSK-HMMS-S	0.8300	94.99	4.7588	0.0392
30 MPa	Proposed Method	**0.3876**	**86.53**	**4.6143**	**0.1840**
	IMD	−1.5907	−384.97	5.3237	0.4586
	MCKD	−5.0318	−342.43	6.7139	1.1615
	MOMEDA	−7.0418	−384.99	7.5768	1.2216
	MTSK-HMMS-S	0.5300	82.73	4.6530	0.0329
40 MPa	Proposed Method	**0.6337**	**88.45**	**4.4190**	**0.1712**
	IMD	−0.2859	−314.42	5.4262	0.4980
	MCKD	−4.6358	−306.32	5.2948	0.7275
	MOMEDA	−13.2150	−315.76	8.2840	1.2327
	MTSK-HMMS-S	0.2100	96.45	4.9312	0.0252

significant challenges in effectively isolating and identifying weak fault signatures from the prevalent high-amplitude background noise.

Subsequently, following the implementation of smoothing operations through Eq. (24), the representation quality in the three-dimensional spatial domain exhibits substantial enhancement, whereby the subtle anomalous impact variations are systematically amplified along specific directional components. Furthermore, the characteristic signals corresponding to each operational condition undergo transformation into distinctive geometric peak-ridge configurations, manifesting continuous topological structures that significantly augment the discriminative capabilities of the system. As evidenced in Fig. 14(a) and Fig. 14(d), the ridge structures associated with suction valve faults and bilateral faults demonstrate pronounced steepness and spatial concentration, wherein multiple peaks intersect and propagate at characteristic angles to form distinctive fault signatures. In contrast, the healthy operational state, depicted in Fig. 14(c), exhibits a uniform and gradual continuous strip distribution pattern, characterized by steady longitudinal progression. The discharge valve fault condition, as shown in Fig. 14(b), manifests as an intricate system of multiple parallel ridges, which, despite their relatively low amplitude, form a dense overlapping structure within a confined bandwidth.

Before quantifying the spatial features through the dynamic ridge tracking algorithm, the core parameters were consistently set as follows: the base step length $s_0 = 1$, the termination coefficient $\tau_{\text{term}} = 0.1$, and the threshold for the squared sum of directional pair weights $\gamma_{\text{term}} = 0.02$. Within the framework of dynamic ridge tracking theory, Fig. 15 illustrates the fundamental discriminative mechanisms through ridge-line contour distributions across distinct operational states. The suction valve failure signature in Fig. 15(a) exhibits characteristic gradient-driven long-range propagation, forming a continuous unidirectional ridge structure aligned with the primary energy transmission axis. This configuration emerges from high directional consistency quantified through Eq. (29), which concentrates weighting coefficients along the dominant orientation. Moreover, when governed by the composite scoring mechanism in Eq. (38), this morphology enhances both mean ridge continuity and energy concentration metrics, thereby generating a structurally integrated principal ridge that manifests dual advantages in the fault response metric.

In contrast, the dual-valve fault condition shown in Fig. 15(d) reveals pronounced polydirectional propagation dynamics, where the primary ridge undergoes rapid steepness transitions within confined spatial intervals. The directional quantization modeling approach (Eq. (28)) detects discrete multi-extremum distributions that necessitate frequent adaptive step-length recalibration per Eq. (33). Although this phenomenon diminishes ridge continuity, the variance compensation mechanism effectively synergizes with elevated peak energy density to maintain diagnostic sensitivity. Its radially dispersed contour clusters fundamentally diverge from the parallel ridge morphology observed in suction valve failures, demonstrating energy path bifurcation inherent to compound fault conditions.

While Fig. 15(b) and Fig. 15(c) exhibit superficially similar ridge amplitudes, their characteristics differ substantially. The discharge valve failure demonstrates dense micro-ridge clusters, identified through adaptive window segmentation (Eq. (26)), significantly increasing the ridge population parameter M in Eq. (38). These fragmented formations originate from frequent termination events under threshold constraints (Eq. (37)), effectively mapping intermittent oscillations from localized fractures. Conversely, the healthy signal manifests isotropic decay where uniformly distributed directional weights produce unidirectional ridge propagation, with the termination condition generating sparse short ridges. This diffuse attenuation pattern reflects the intrinsic state of the system without abnormal excitation.

A comparative analysis in Fig. 16 reveals the limitations of current diagnostic indicators. While kurtosis identifies high-energy dual valve faults, its sensitivity to other conditions is poor. Similarly, local energy and information entropy fail to establish

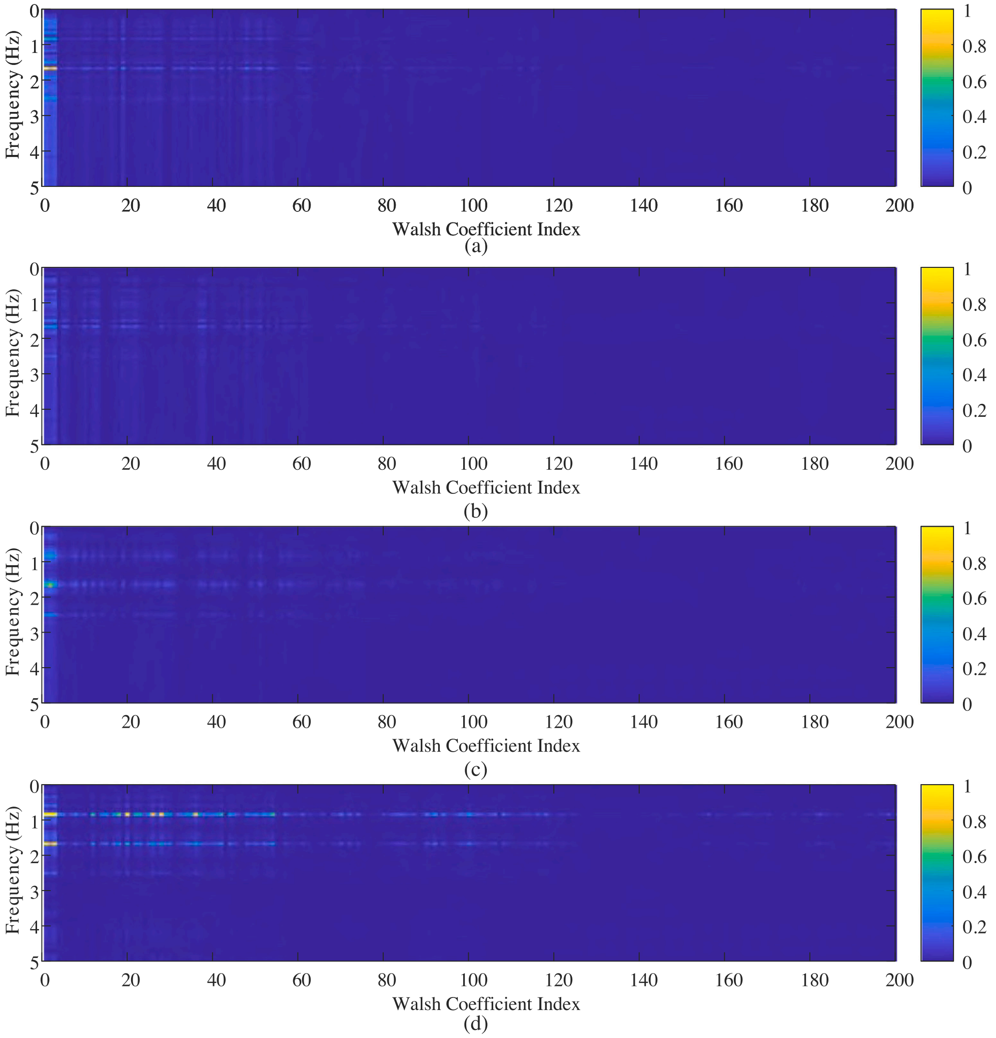

Fig. 13. Feature distribution of dual-domain matrices at 10 MPa. (a) Suction valve fault (b) Discharge valve fault (c) Healthy condition (d) Dual valve fault.

clear boundaries for discharge valve faults due to amplitude overlaps with healthy signals. In contrast, our multidimensional methodology (Fig. 16(d)) effectively eliminates parametric variations, maintaining a near-zero score for healthy baselines. This approach overcomes the omissions seen in traditional metrics, enabling clear separation across all operational states.

Finally, to further benchmark the proposed framework against cutting-edge indicators from recent literature, we compared our method with Fuzzy Entropy [39], Envelope Kurtosis [40], and Margin Factor [41], and the Vibration Grading Weighted Index (VGWI) [25] derived from the MTSK-HMMS-S reconstructed signals. To evaluate statistical stability, the 12-second raw signal was segmented into 40 slices with a 50% overlap between adjacent frames. Fig. 17 displays the metric distributions for the five methods across four health states. As identified from the y-axis labels, panels (a)–(d) correspond to the comparative methods, while panel (e) represents our proposed Ridge Line Score. Note that the values of Fuzzy Entropy have been normalized due to their small magnitude, which preserves the relative relationships between different health states. It is evident that the comparative methods (such as Fuzzy Entropy, Envelope Kurtosis, and Margin Factor) exhibit large variance and significant overlap between fault categories, failing to provide a clear boundary for diagnosis. While VGWI (Fig. 17(d)) demonstrates relatively better clustering than the aforementioned traditional metrics, it struggles to establish a monotonic relationship with fault severity. As quantified in Table 2, the VGWI value for the dual valve fault condition at 10 MPa (1.02) is paradoxically lower than those of single valve faults (1.12 and 1.08), which heavily confounds severity assessment.

In contrast, the proposed method demonstrates superior stability with minimal intra-class variance. More importantly, as quantified in Table 2, our metric exhibits a distinct hierarchical order correlated with fault severity: the mean values strictly ascend from the Healthy state (0.22) to the Discharge Fault (0.73), Suction Fault (1.01), and Dual Fault (2.38). This specific ranking serves as a physical validation of the result correctness: the fact that suction fault scores exceed discharge fault scores correlates with

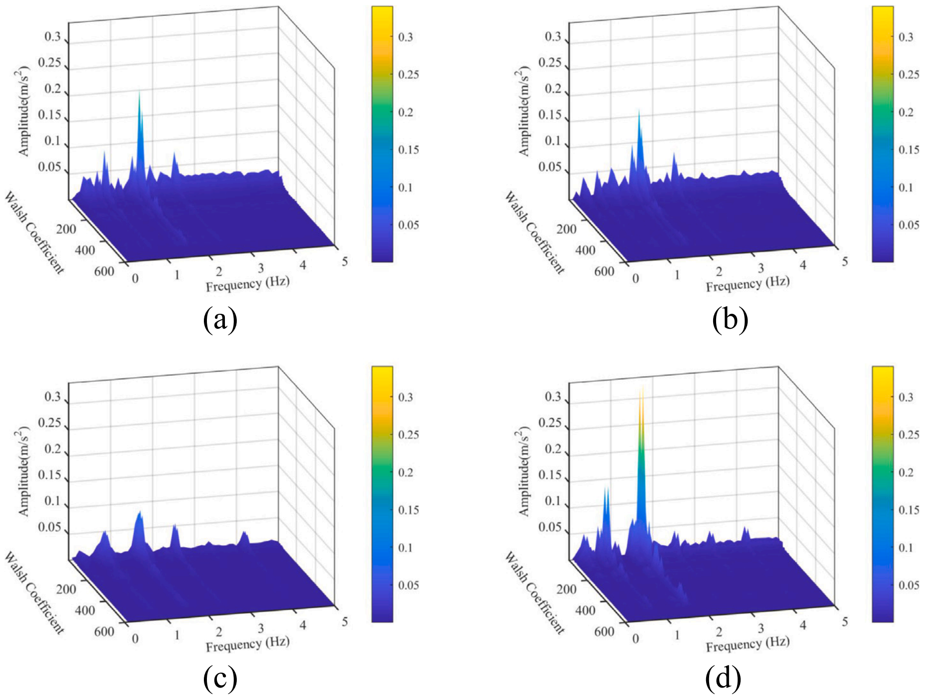

Fig. 14. 3D heatmap of the feature domain of the signals at 10 Mpa: (a) Suction valve fault (b) Discharge valve fault (c) Healthy condition (d) Dual valve fault.

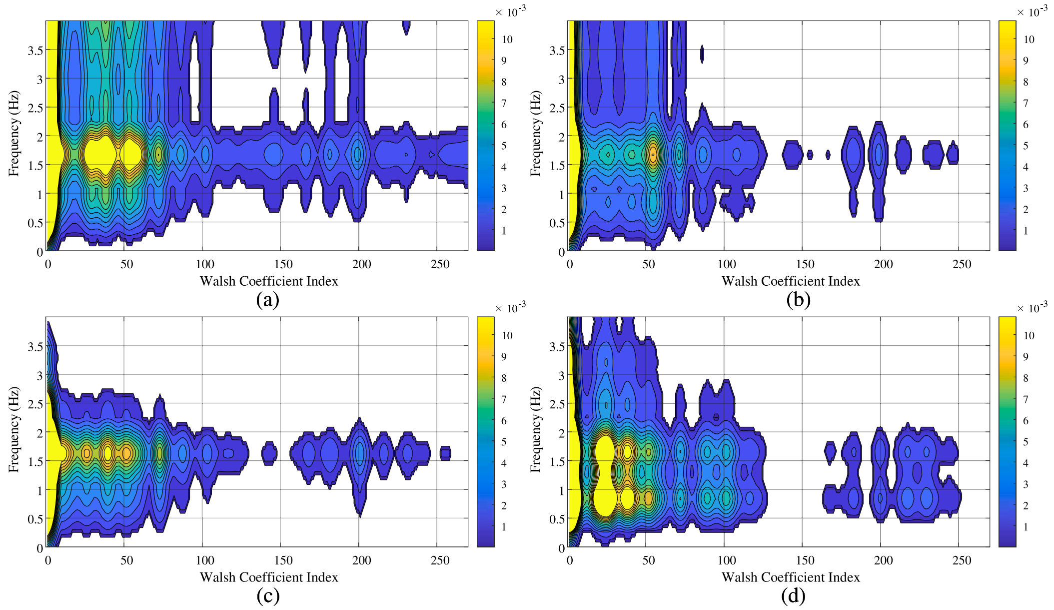

Fig. 15. Ridge-line distributions in feature domain at 10 MPa. (a) Suction valve fault (b) Discharge valve fault (c) Healthy condition (d) Dual valve fault.

the sensor's closer proximity to the suction valve assembly which facilitates stronger signal capture, while the peak value for dual faults accurately reflects the superposition of multiple impact sources. This monotonicity enables our method to not only distinguish between healthy and faulty states but also to quantify the severity and complexity of the fault evolution—a capability that the other metrics lack.

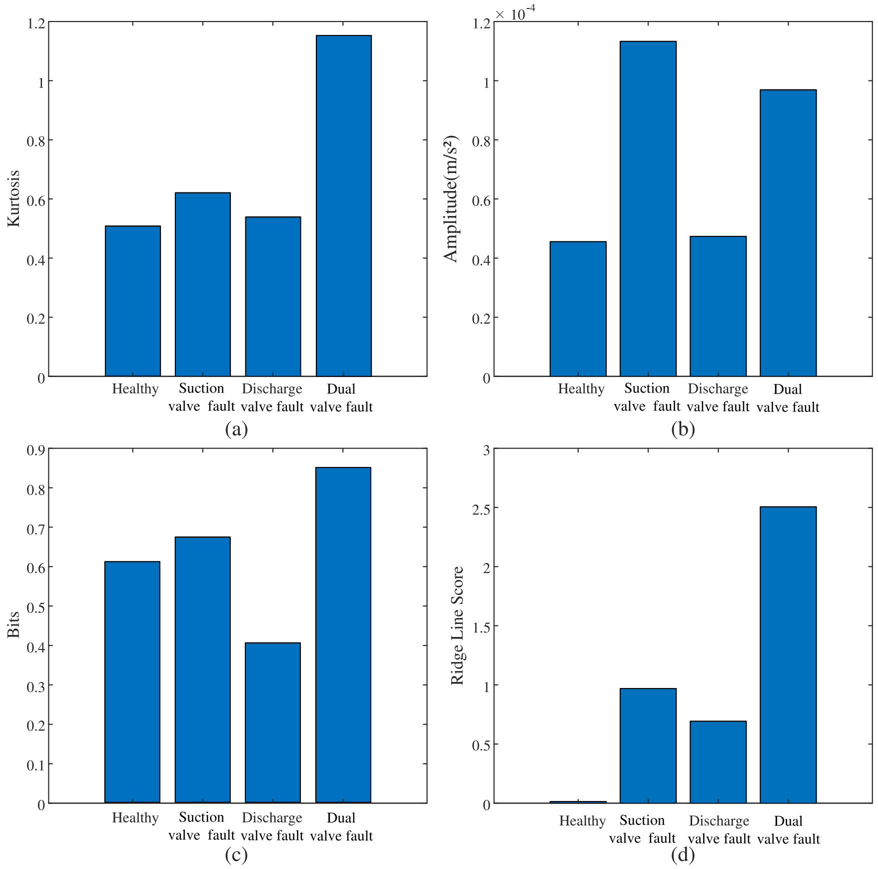

Fig. 16. Comparative analysis of diagnostic signals at 10 MPa. (a) Kurtosis (b) Local energy (c) Information entropy (d) Ridge line score.

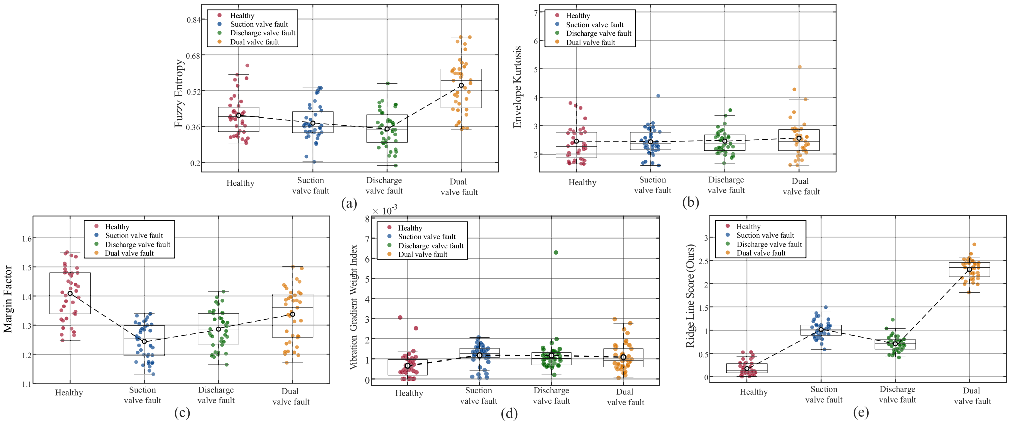

Fig. 17. Scatter plot comparison of fault indicators across four health states at 10 MPa: (a) Fuzzy Entropy (b) Envelope Kurtosis (c) Margin Factor (d) VGWI (e) The proposed method.

4.2.2. Case study II

To explore the influence of elevated pressure on hydraulic pump vibration signatures, a dedicated experimental campaign was executed under rigorously controlled conditions. The operating pressure of the multi-cylinder hydraulic pump system was set and maintained at a constant 20 MPa for this investigation, focusing on vibration signal acquisition from its first cylinder. Consistent with observations at 10 MPa, the system impact period remained stable at 1.2 s (fundamental frequency: 0.83 Hz). As shown by the blue waveforms in Fig. 21, time-domain signals for suction valve faults, discharge valve faults, healthy condition, and dual valve

Table 2
Mean values of different fault indicators across four health states under varying discharge pressures.

Pressure	Health state	Fuzzy entropy	Envelope kurtosis	Margin factor	VGWI ($\times 10^{-3}$)	Ridge score
10 MPa	Healthy	0.41	2.61	1.41	0.55	**0.22**
	Suction Fault	0.38	2.60	1.24	1.12	**1.01**
	Discharge Fault	0.35	2.67	1.29	1.08	**0.73**
	Dual Fault	0.55	2.76	1.33	1.02	**2.38**
20 MPa	Healthy	0.45	2.59	1.43	0.59	**0.22**
	Suction Fault	0.77	2.24	1.45	1.13	**0.51**
	Discharge Fault	0.70	2.38	1.48	1.15	**0.39**
	Dual Fault	0.59	2.32	1.59	1.08	**0.78**
30 MPa	Healthy	0.47	2.38	1.41	0.62	**0.61**
	Suction Fault	0.65	2.47	1.53	1.24	**1.57**
	Discharge Fault	0.67	2.17	1.49	1.09	**1.28**
	Dual Fault	0.64	2.11	1.58	1.13	**3.50**
40 MPa	Healthy	0.46	2.32	1.38	0.71	**0.22**
	Suction Fault	0.64	2.23	1.52	1.13	**1.19**
	Discharge Fault	0.69	2.17	1.49	1.12	**0.74**
	Dual Fault	0.55	2.02	1.55	1.09	**1.75**

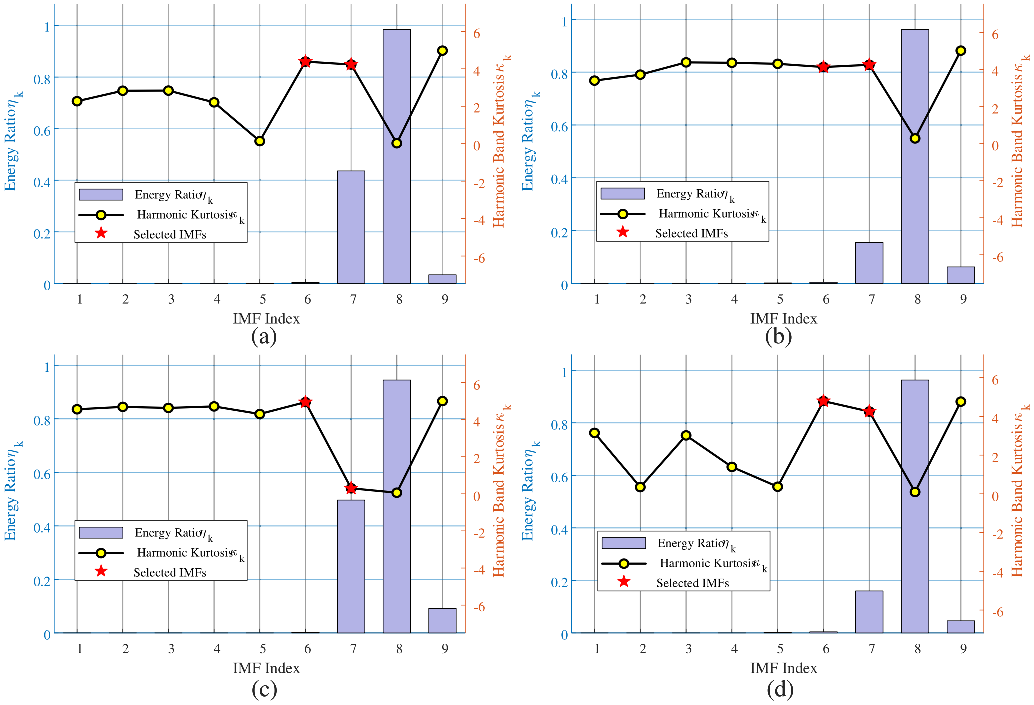

Fig. 18. IMF selection criteria analysis using energy ratio and kurtosis values: (a) Suction valve fault; (b) Discharge valve fault (c) Healthy operation (d) Dual valve fault.

faults exhibit persistent visual indistinguishability, manifesting as periodic oscillations with highly aliased amplitude and phase characteristics, thereby impeding conventional diagnostic differentiation.

Subsequently, Variational Mode Decomposition (VMD) was also used to process and analyze signals from four different sources. Fig. 18 reveals the energy ratio and spectral kurtosis distributions at 20 MPa. Notably, IMF5-8 display a characteristic steep energy gradient progression, with IMF8 demonstrating the most pronounced energy concentration during valve fault conditions. At IMF7 (Fig. 18(c)), the healthy condition exhibits a substantially higher energy ratio than fault conditions, while simultaneously maintaining lower spectral kurtosis values, establishing an inverse correlation trend. This pressure-dependent behavior corresponds to the weight allocation patterns in Fig. 19, where a significant shift toward IMF7 weighting occurs across all conditions compared to 10 MPa. Crucially, healthy signals demonstrate markedly higher weight concentration in IMF7 than fault conditions.

Consistent with the validation protocol established in the previous case study, we repeated the parameter sensitivity analysis for the 20 MPa working condition to ascertain the generalization capability of the proposed framework under higher discharge pressures. As depicted in Fig. 20, the stability trends of the reconstruction quality remain consistent with those in Case I. The SNR

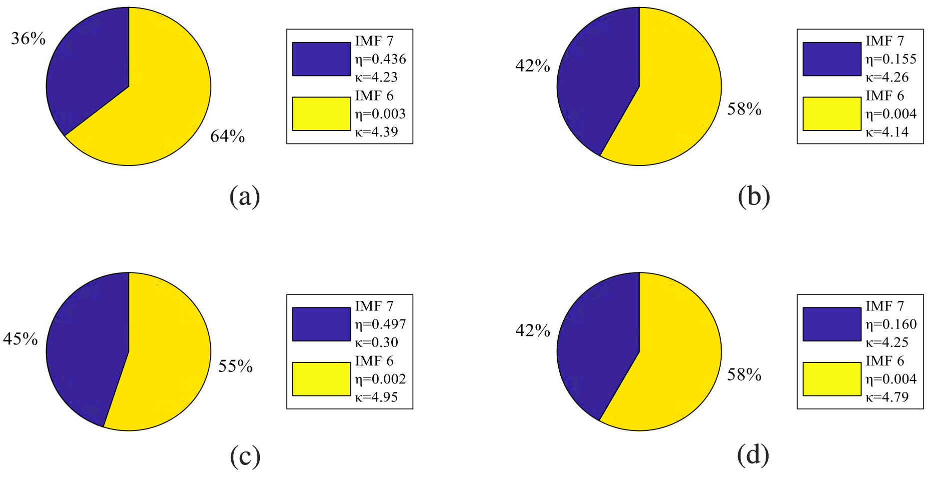

Fig. 19. Optimized weighting coefficients for IMF signal reconstruction: (a) Suction valve fault (b) Discharge valve fault (c) Healthy condition (d) Dual valve fault.

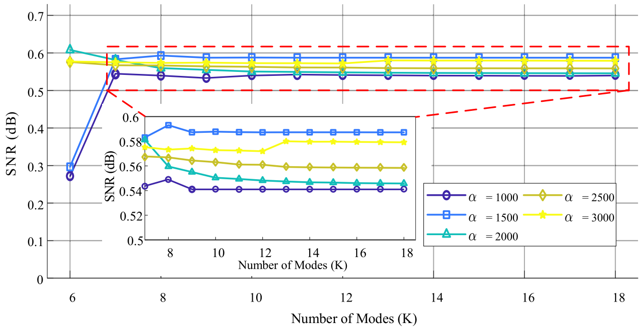

Fig. 20. Impact of mode number K and penalty factor α on the SNR of the reconstructed signal under 20 MPa.

is relatively low for the penalty factors of 1000 and 1500 when $K = 6$. For $K \geq 7$, the SNR increases rapidly and reaches a stable state with almost no variation as K changes, and the differences among the curves of different penalty factors are negligible. This confirms that the algorithm maintains its robustness and does not require re-tuning even as the operating pressure doubles.

The weight distribution characteristics directly influence the reconstructed signals in Fig. 21. The IMF7-dominated reconstruction mechanism effectively isolates background inertial oscillations under high pressure, enhancing pulse SNR for fault conditions. Conversely, healthy signals exhibit distinct physical manifestations: their vibration waveforms display weaker periodicity and lower amplitudes, reflecting the intrinsic system state without fault excitations. This contrast demonstrates the framework's capacity to amplify subtle operational deviations under varying pressure regimes.

The optimized reconstructed spectra demonstrate significantly enhanced separation between fault and healthy signals in the frequency domain, as evidenced in the comparative spectral analysis of Fig. 22. Examination of Fig. 22(c) reveals that healthy signals maintain exclusively low-order smooth responses concentrated within the low-frequency band. Conversely, Fig. 22(a), Fig. 22(b) and Fig. 22(d) respectively depicting suction valve fault, discharge valve fault and dual valve fault conditions collectively exhibit pronounced multi-order harmonic excitation phenomena. Each fault signature excites multiple harmonic components beyond the third order at the fundamental vibration frequency, with characteristic response amplitudes substantially exceeding those observed in healthy baselines. This systematic spectral divergence confirms the reconstruction methodology's efficacy in amplifying diagnostically critical distinctions between operational states.

To visualize these improvements temporally, Fig. 23 illustrates the time-domain comparison of the reconstructed signals under the 20 MPa condition. Consistent with the results in Case I, the proposed method (Fig. 23(a)) maintains a stable baseline with distinct periodic impulses, effectively mitigating the background interference. Conversely, the IMD method (Fig. 23(b)) continues to exhibit significant waveform distortion, where the extracted signal intensity fluctuates irregularly due to mode mixing. Additionally, the MCKD and MOMEDA methods (Fig. 23(c)–(d)) begin to show a denser noise floor between impacts compared to the 10 MPa case. The MTSK-HMMS-S reconstruction (Fig. 23(e)) further highlights its characteristics under elevated pressure. While it successfully

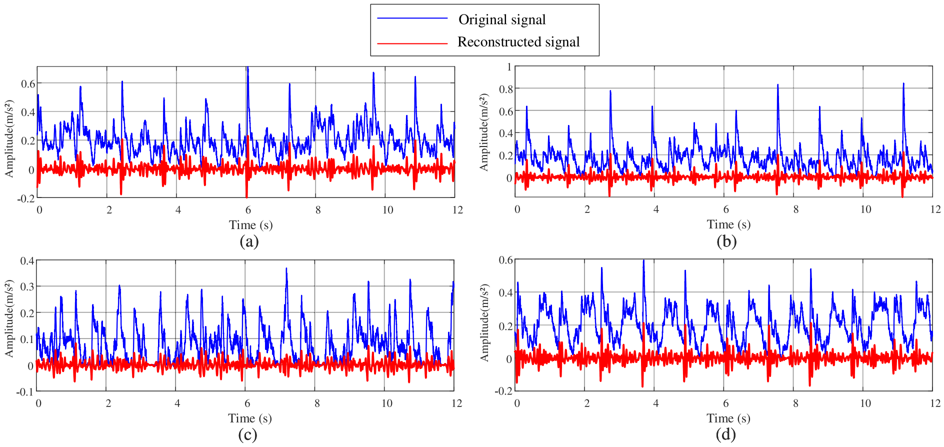

Fig. 21. Original versus reconstructed signals: (a) Suction valve fault (b) Discharge valve fault (c) Healthy condition (d) Dual valve fault.

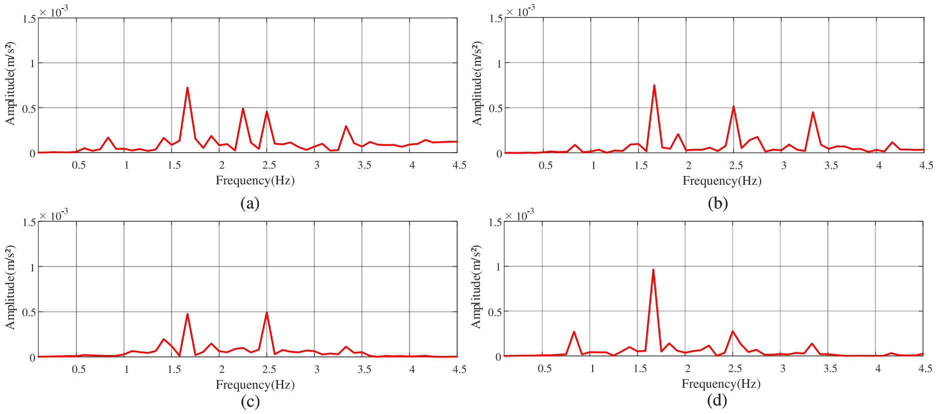

Fig. 22. Spectral analysis of reconstructed signals at 20 MPa: (a) Suction valve fault (b) Discharge valve fault (c) Healthy condition (d) Dual valve fault.

continues to suppress inter-impact background noise, the amplitude variance between adjacent periodic peaks becomes significantly more erratic. As higher discharge pressures induce slight kinematic non-linearities, the fixed temporal template of the algorithm inadvertently discards valid transient dynamic energy that slightly deviates from the theoretical period, thereby distorting the physical consistency of the mechanical impacts. These visual observations are corroborated by the quantitative data in Table 1. Although MTSK-HMMS-S maintains artificially low MFE (0.0392) and high NRR due to its aggressive inter-impact truncation, its ESNR drops below that of the proposed method (0.8300 dB vs. 0.9773 dB), and its SE increases. This quantitative shift reflects the algorithm's growing inability to consistently preserve the physical periodic energy envelope under elevated pressure. Conversely, the proposed method achieves a superior balance, outperforming comparative approaches in terms of both signal purity and structural regularity.

The feature domain constructed by the proposed method reveals diagnostically significant geometric distinctions under elevated pressure. As shown in Fig. 24, compared to the dispersed distributions observed at 10 MPa, the ridge structures exhibit pronounced steepness intensification with energy foci converging toward the intrinsic frequency axis. Distinct morphological shifts emerge in fault signatures: the feature domains of suction valve failure and discharge valve failure are manifested as isolated conical peaks, while the dual valve fault signal shows a more drastic transformation, integrating obvious multi-layer ridges and terraces from the originally radially dispersed mountain clusters. Conversely, healthy states maintain consistent gentle slopes, amplifying the diagnosable dynamic differences.

The ridge line contour distributions depicted in Fig. 25 establish fundamental diagnostic mechanisms within the dynamic ridge tracking paradigm. Comparative analysis reveals that suction valve and discharge valve faults exhibit structurally congruent manifestations, demonstrating equivalent structural acutance toward multifocal protrusions with localized regions developing densely clustered micro-ridge scatter patterns at significantly elevated densities, illustrated in Fig. 25(a) and Fig. 25(b). Healthy conditions consistently maintain low-gradient, sparsely distributed point topologies, confirming inherently low-amplitude oscillatory characteristics of the system's baseline dynamics, as demonstrated by Fig. 25(c). In contrast, compound dual valve faults

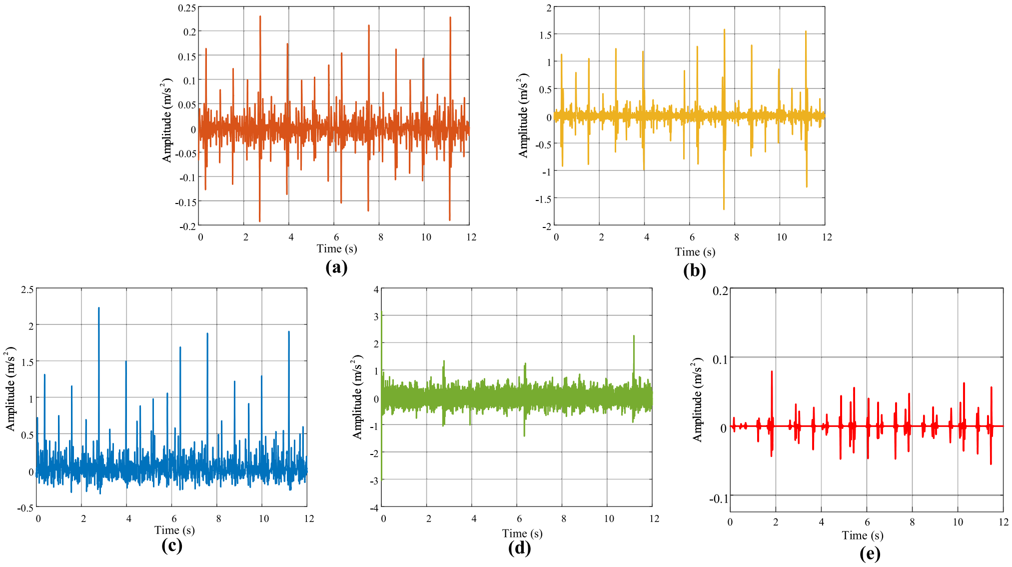

Fig. 23. Comparison of reconstructed time-domain signals at 20 MPa: (a) The proposed method (b) IMD (c) MCKD (d) MOMEDA (e) MTSK-HMMS-S.

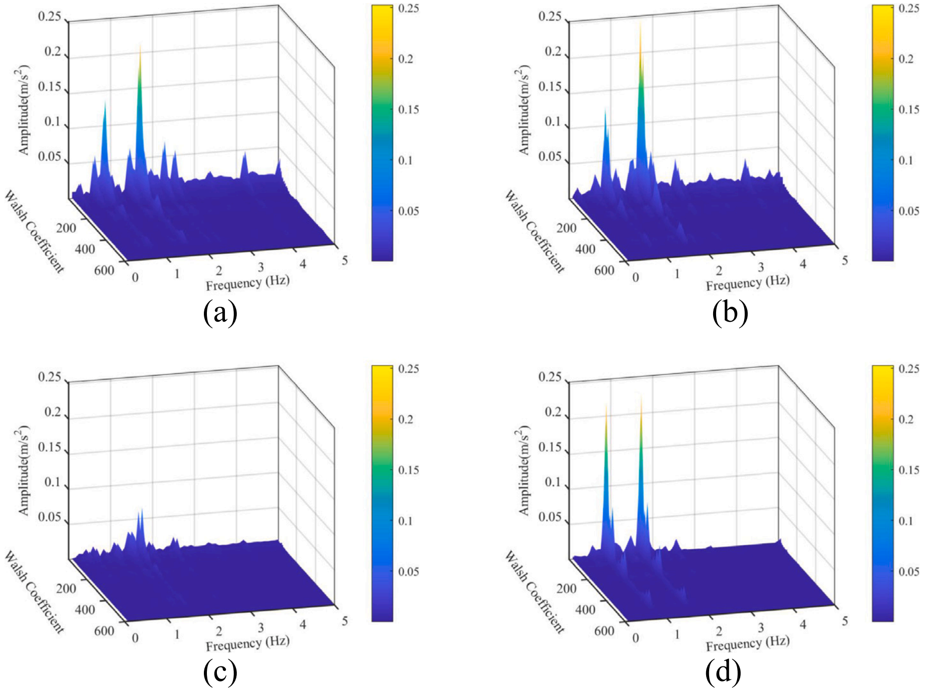

Fig. 24. 3D heatmap of the feature domain of the signals at 20 Mpa: (a) Suction valve fault (b) Discharge valve fault (c) Healthy condition (d) Dual valve fault.

generate extensive high-coverage ridge domains characterized by polycentric primary-ridge configurations, evident in Fig. 25(d). Crucially, increased pressure regimes mechanically amplify geometric differentiation within feature spaces, enhancing state-specific discriminability through intensified fault-response signatures.

Fig. 26 demonstrates the fundamental divergence in performance under higher pressure. Conventional metrics exhibit significant diagnostic crossover: kurtosis loses sensitivity to suction and dual faults, while local energy and information entropy blur the distinction between discharge faults and healthy states due to energy dispersion and amplitude aliasing (Fig. 26(a)–(c)). Conversely, the proposed ridge line scoring (Fig. 26(d)) exhibits exceptional pressure-invariant robustness. The healthy baseline remains

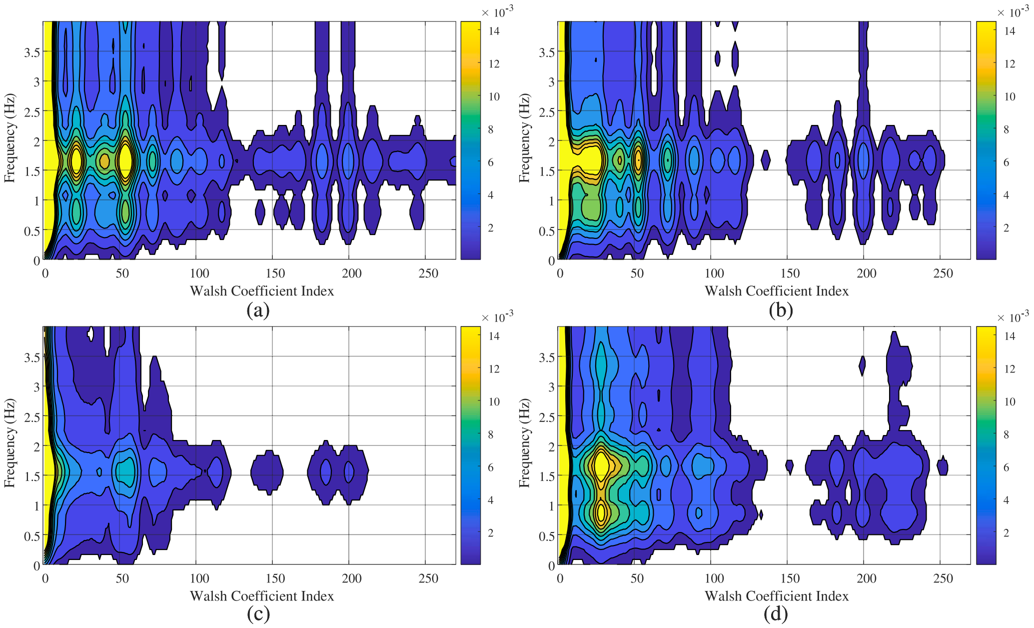

Fig. 25. Ridge-line distributions in feature domain at 20 MPa. (a) Suction valve fault (b) Discharge valve fault (c) Healthy condition (d) Dual valve fault.

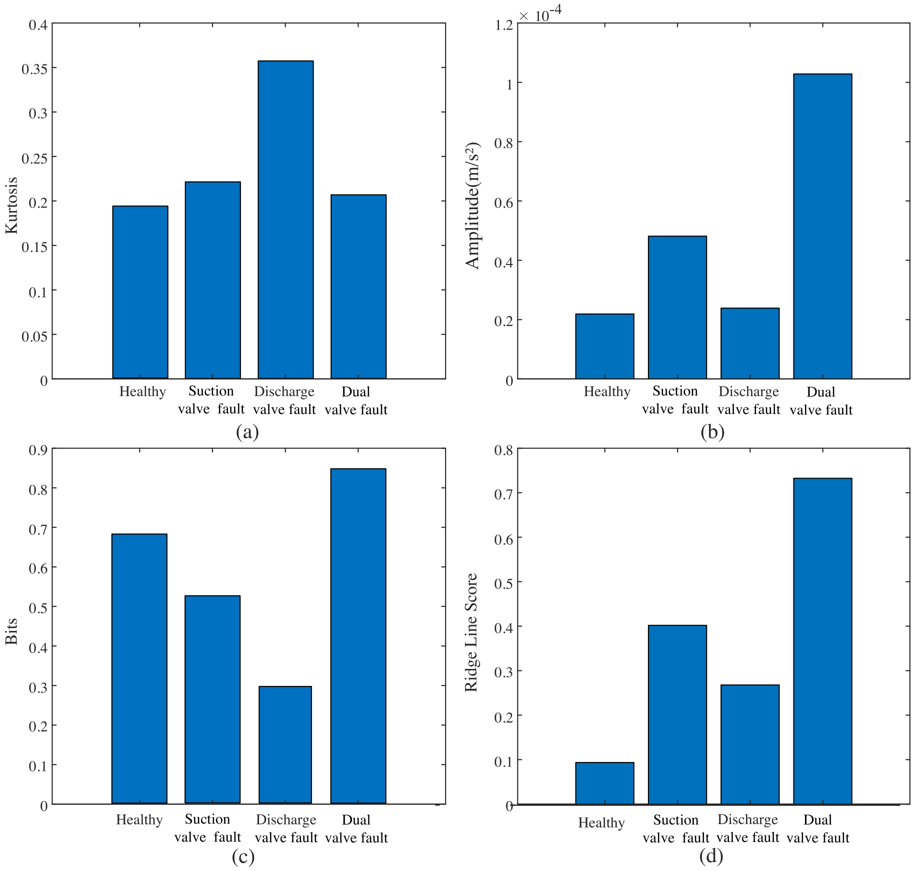

Fig. 26. Comparative analysis of diagnostic signals at 20 MPa. (a) Kurtosis (b) Local energy (c) Information entropy (d) Ridge line score.

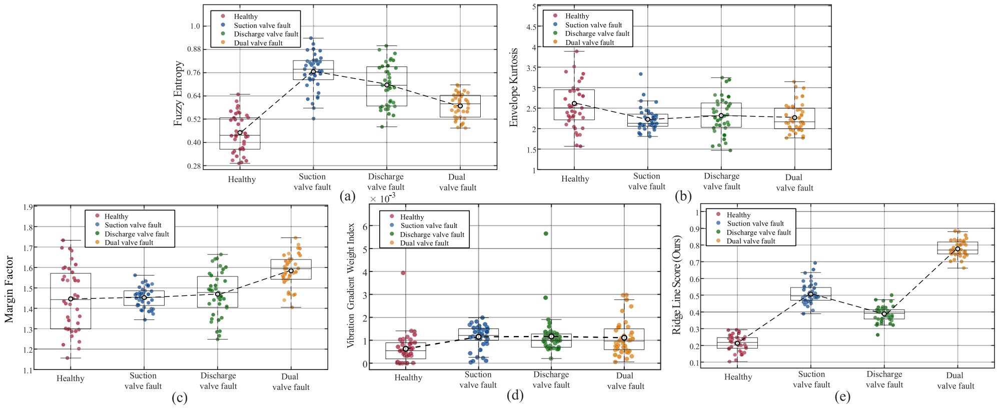

Fig. 27. Scatter plot comparison of fault indicators across four health states at 20 MPa: (a) Fuzzy Entropy (b) Envelope Kurtosis (c) Margin Factor (d) VGWI (e) The proposed method.

converged near zero, while the three fault categories maintain distinct discriminability, ranked in descending order from Dual Faults to Suction Faults and Discharge Faults, verifying the effectiveness of the method.

Extending the analysis to the 20 MPa condition (Fig. 27), the limitations of the baseline methods become more pronounced. As observed in panels (a)–(d), the comparative metrics suffer from severe feature aliasing. Specifically, while VGWI (panel d) manages to separate the healthy baseline from the fault states better than Fuzzy Entropy, Envelope Kurtosis, and Margin Factor, it exhibits a counterintuitive severity response: the dual valve fault metric (1.08) is lower than both single valve faults (1.13 and 1.15), failing to reflect the compounded severity of multi-source failures. Conversely, the proposed method (Fig. 27(e)) maintains precise stratification among all health states. Quantitative results in Table 2 further validate this fine-grained resolution: the Ridge Line Score captures the subtle evolution of fault severity, rising stepwise from 0.22 (Healthy) to 0.39 (Discharge Fault), 0.51 (Suction Fault), and 0.78 (Dual Fault). This confirms that the proposed metric retains high diagnostic sensitivity even when the separation margin narrows.

4.2.3. Case study III

An experimental investigation was conducted to characterize vibration signatures of hydraulic pumps under stepwise pressurization, maintaining identical operational parameters as Case II while dynamically elevating pressure to 30 MPa. Each pressure stage was stabilized for a consistent duration, with continuous vibration signals acquired from the first cylinder. As shown in Fig. 31, time-domain analysis reveals that signals from all three fault conditions and the healthy condition exhibit more pronounced impulsive characteristics under this regime. Notably, the waveforms of suction valve fault and discharge valve fault signals remain highly similar, as illustrated in Fig. 31(a) and Fig. 31(b). The healthy condition signals demonstrate significantly lower overall amplitudes compared to dual valve fault signals, which, due to multi-source fault coupling, manifest as alternating periodic vibrations with large-amplitude pulses of both long and short single-event durations in the time domain, as shown in Fig. 31(c) and Fig. 31(d).

Subsequently, VMD was applied to process signals under this pressure condition, and Fig. 28 displays the energy ratio and spectral kurtosis distributions, yielding more distinct IMF selection characteristics compared to Case II. The 30 MPa dataset exhibits universally higher kurtosis values across all components. Notably, the healthy condition in Fig. 28(c) demonstrates a more pronounced energy ratio in IMF7 than other fault states, whereas fault conditions (Fig. 28(a), Fig. 28(b) and Fig. 28(d)) manifest similar energy distributions, indicating that faults exhibit enhanced sensitivity to pressure fluctuations with analogous responses primarily reflected in specific components. This dynamic IMF behavior correlates with the time-varying load profile, as energy concentration does not impose significant impacts on system baseline vibrations, thereby reflecting the system's adaptive response to incremental pressurization.

As illustrated in Fig. 29, the optimized weighting coefficients for IMF signal reconstruction exhibit a distinct ESK-dependent distribution compared to Case II. The 30 MPa dataset reveals a dynamic rebalancing among IMF5-7, where fault conditions (Fig. 29(a), Fig. 29(b) and Fig. 29(d)) demonstrate notable similarity in weight proportions across components during stepwise pressurization, indicating consistent impacts of different valve faults on ESK metrics under dynamic loading. In contrast, the healthy condition (Fig. 29(c)) shows a divergent weighting pattern, favoring mid-frequency information and exhibiting reduced baseline oscillations.

The signal reconstruction results in Fig. 31 further validate the dynamic weighting effect. While suction and discharge valve fault signals (Fig. 31(a), Fig. 31(b)) maintain waveform similarity, this feature is also reflected in their frequency-domain representations, as shown in Fig. 32(a) and Fig. 32(b). The reconstructed healthy condition signals (Fig. 31(c)) retain lower impulsive amplitudes due to reduced low-frequency weighting, reflecting baseline dynamic adjustments to incremental loading—this is also manifested as fewer vibration frequency order responses in the frequency domain. Notably, the reconstructed dual valve fault signals (Fig. 31(d)) do not exhibit the complex pulse characteristics with alternating long and short cycles observed in raw signals. Instead,

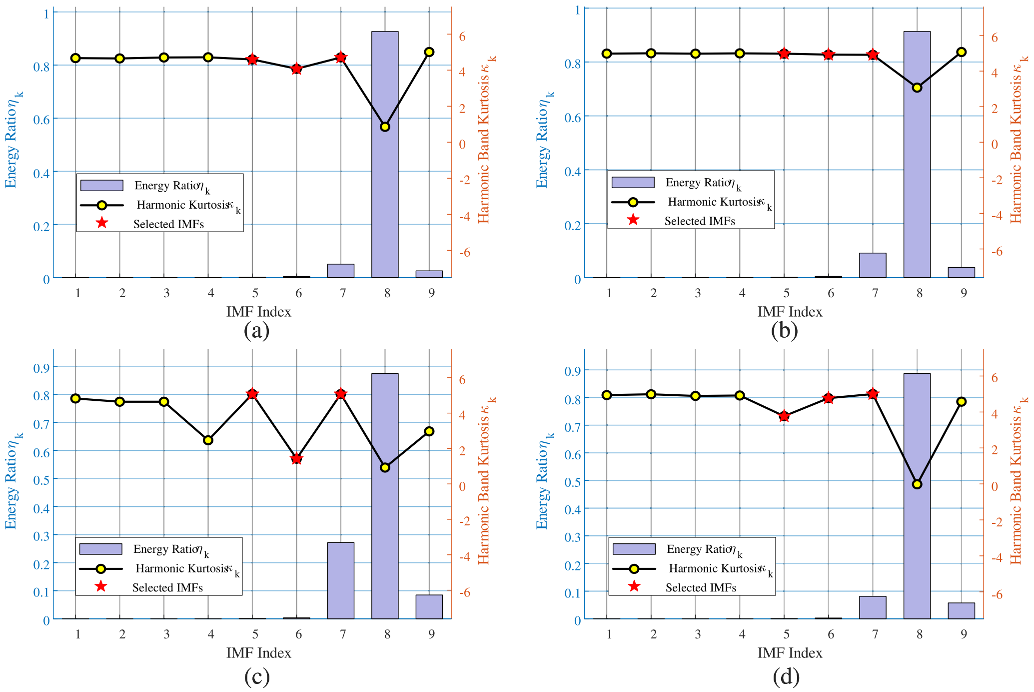

Fig. 28. IMF selection criteria analysis using energy ratio and kurtosis values: (a) Suction valve fault (b) Discharge valve fault (c) Healthy operation (d) Dual valve fault.

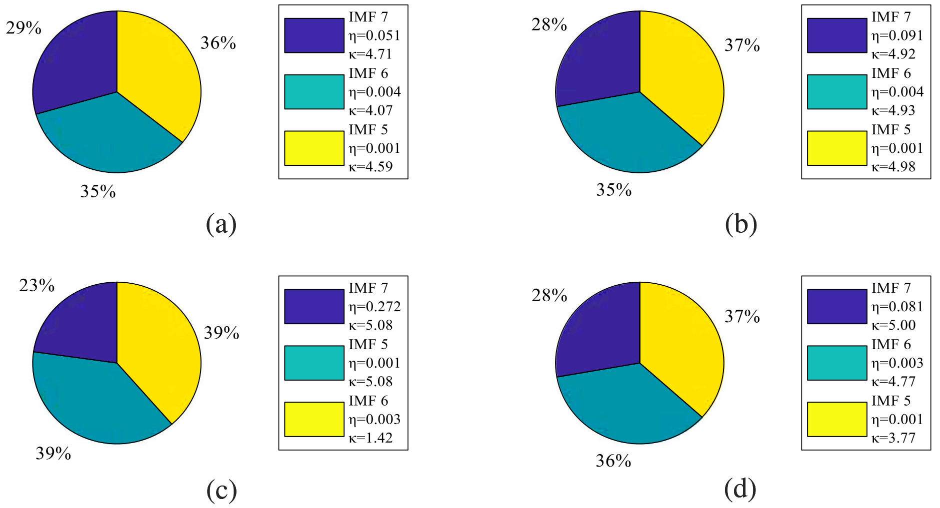

Fig. 29. Optimized weighting coefficients for IMF signal reconstruction: (a) Suction valve fault (b) Discharge valve fault (c) Healthy condition (d) Dual valve fault.

they resemble single-fault signals, with significantly reduced noise and sustained high amplitude impulses, corresponding to more abundant vibration frequency orders and larger amplitude features in the frequency domain.

Continuing the rigorous stability assessment, we conducted the sensitivity analysis for the 30 MPa discharge pressure to evaluate the proposed framework under the high-pressure condition. As shown in Fig. 30, the SNR curves for all penalty factors maintain excellent stability across the entire range of K values. Although slight differences exist among the curves corresponding to different penalty factors, the magnitude of such differences is small and insignificant. This confirms that the method's performance is insensitive to parameter initialization even under high-load states.

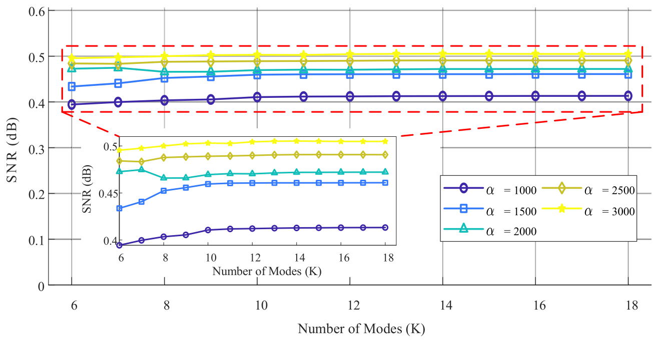

Fig. 30. Impact of mode number K and penalty factor α on the SNR of the reconstructed signal under 30 MPa.

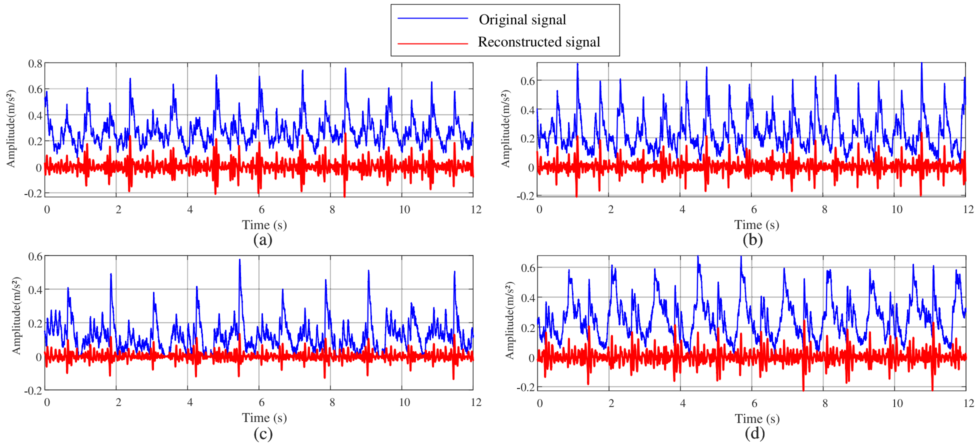

Fig. 31. Original versus reconstructed signals: (a) Suction valve fault (b) Discharge valve fault (c) Healthy condition (d) Dual valve fault.

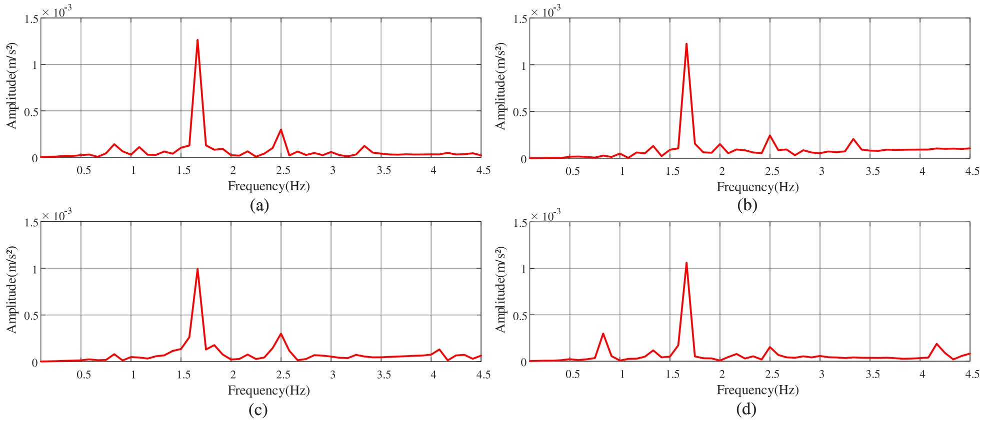

Fig. 32. Spectral analysis of reconstructed signals at 30 MPa: (a) Suction valve fault (b) Discharge valve fault (c) Healthy condition (d) Dual valve fault.

Validating these spectral characteristics in the temporal domain, Fig. 33 compares the signal reconstruction performance under the 30 MPa condition. As the discharge pressure rises, the background noise in the raw signal intensifies. The proposed method (Fig. 33(a)) remains robust, extracting clean fault impulses with consistent morphology. In comparison, the IMD method (Fig. 33(b)) produces a reconstruction with irregular peak shapes and excessive amplitude fluctuations, failing to preserve the physical consistency of the valve impacts. Furthermore, the MCKD and MOMEDA methods (Fig. 33(c)–(d)) struggle to separate the fault transients from the heavy background interference. Under the 30 MPa high-noise regime, the MTSK-HMMS-S method (Fig. 33(e)) correctly anchors the periodic intervals of the fault but shows a degradation in waveform fidelity. The physical magnitudes

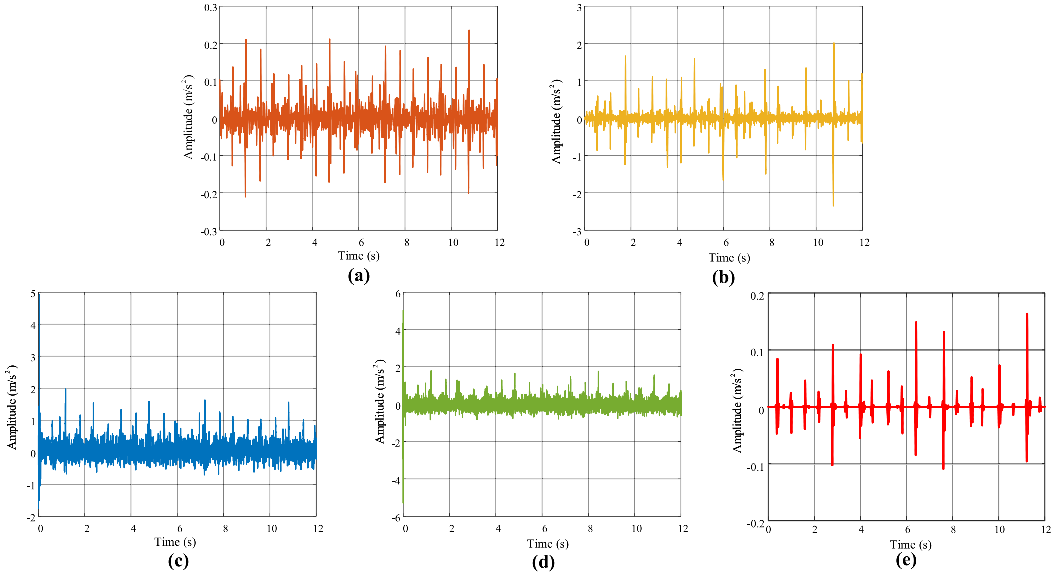

Fig. 33. Comparison of reconstructed time-domain signals at 30 MPa: (a) The proposed method (b) IMD (c) MCKD (d) MOMEDA (e) MTSK-HMMS-S.

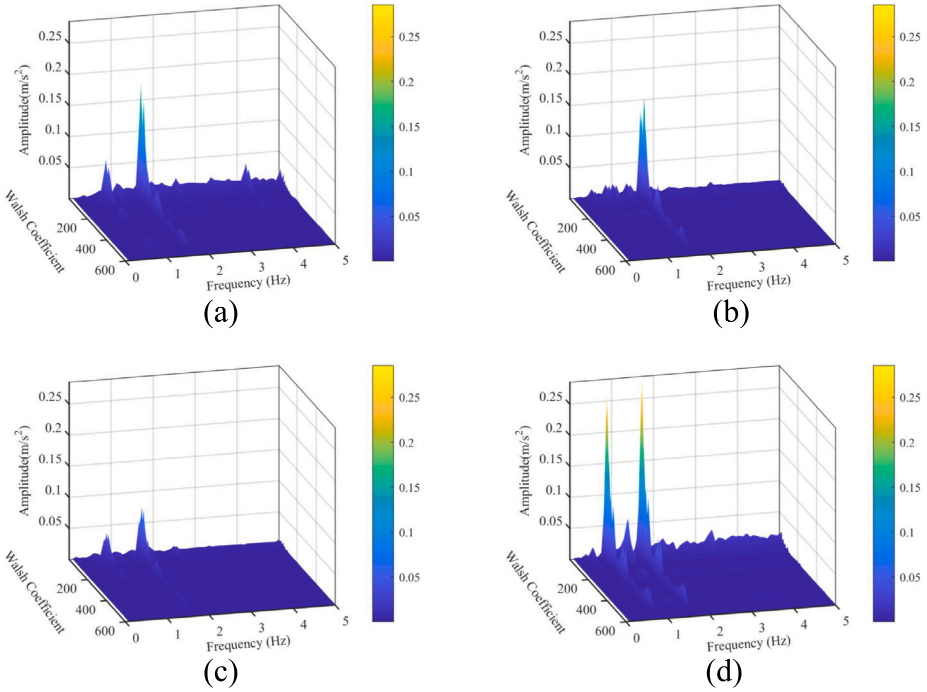

Fig. 34. 3D heatmap of the feature domain of the signals at 30 Mpa: (a) Suction valve fault (b) Discharge valve fault (c) Healthy condition (d) Dual valve fault.

of the impulses are heavily distorted, with some peaks unnaturally amplified while adjacent ones are diminished. This occurs because its purely time-domain shifting mechanism struggles to fully accommodate the complex harmonic resonances and structural modulations excited under high pressure, leading to an incomplete and visually chaotic fault morphology. Table 1 quantitatively highlights this performance gap. While MTSK-HMMS-S maintains a positive ESNR, its NRR significantly drops to 82.73% (lower than the proposed method's 86.53%), and its SE remains higher. This mathematically proves that purely time-domain shifting struggles to

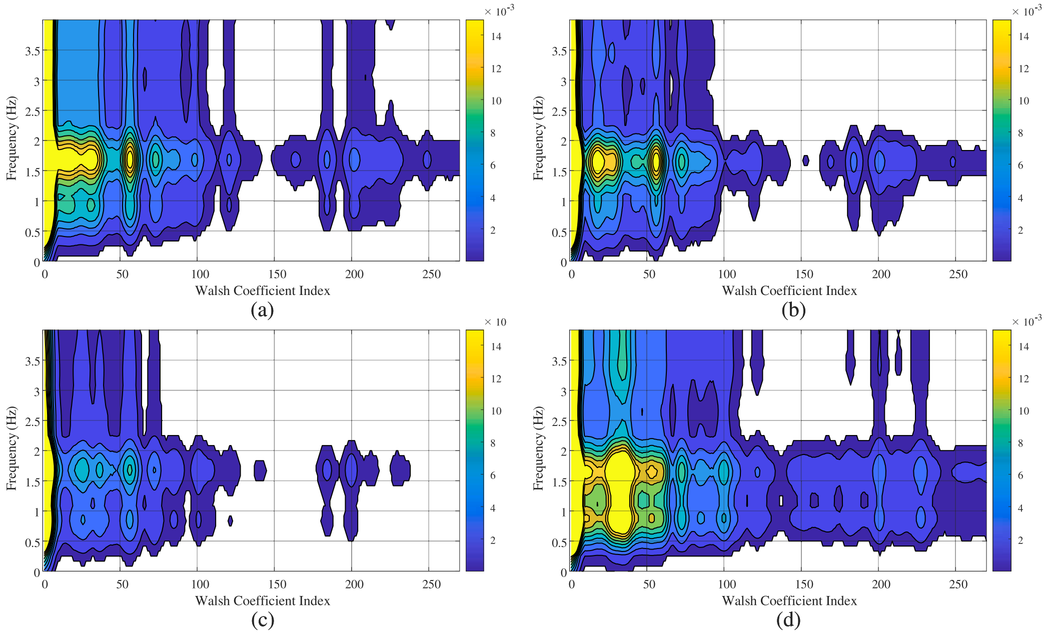

Fig. 35. Ridge-line distributions in feature domain at 30 MPa. (a) Suction valve fault (b) Discharge valve fault (c) Healthy condition (d) Dual valve fault.

suppress the complex in-band harmonic resonances excited at 30 MPa. Meanwhile, the proposed method retains optimal structural complexity scores (SE=4.6143) and positive ESNR, indicating superior, adaptive noise suppression without waveform distortion.

Following the construction of the feature domain, as shown in Fig. 34, suction valve faults manifest as distinct multi-layered energy terraces, whereas discharge valve faults exhibit a dominant conical peak centered at the second-order vibration frequency with minor satellite clusters. The dual valve fault signal (Fig. 34(d)) is characterized by a bifurcated ridge structure with enhanced radial dispersion, while healthy-state heatmaps (Fig. 34(c)) present shallow-gradient, energy-depleted ridges. This pressure-rate-sensitive fault mechanism is further reflected in ridge-line distributions: suction and discharge valve faults (Fig. 35(a), Fig. 35(b)) display sparse micro-ridge peaks, whereas dual valve faults (Fig. 35(d)) form interconnected ridge clusters. Healthy conditions (Fig. 35(c)) retain sparse, low-amplitude ridge points, indicative of baseline stability under incremental loading.

The superiority of the proposed method in dynamic scenarios is highlighted in Fig. 36. Conventional kurtosis and entropy fail to discriminate between fault states and healthy baselines (Fig. 36(a)–(b)). Although local energy shows a similar ranking trend to our method, it lacks a sufficient safety margin between healthy states and discharge valve faults. The ridge line score (Fig. 36(d)) resolves this by maintaining strict separability, ensuring that even minor discharge faults are clearly distinguishable from the healthy state.

To rigorously test this superiority against state-of-the-art baselines, the fault indicator comparison for the 30 MPa case is visualized in Fig. 37. A closer inspection of the comparative metrics, particularly panels (c) and (d), reveals critical limitations despite the increased pressure. While panel (c) begins to exhibit a rough separation between the healthy and faulty states, it lacks the resolution to distinguish between specific failure modes, leaving the suction and discharge valve fault clusters heavily entangled, and exhibits excessive variance. Similarly, although VGWI in panel (d) shows tighter clustering, it again fails the monotonicity test for fault severity, assigning a lower score to the dual valve fault (1.13) than to the suction valve fault (1.24).

In stark contrast, the proposed method (Fig. 37(e)) yields a highly separable and stable distribution. The specific mean values listed in Table 2 highlight a clear ascending order corresponding to fault severity: the healthy state registers the lowest score (0.61), followed by the discharge valve fault (1.28) and suction valve fault (1.57), with the dual valve fault exhibiting the highest values (3.50). This wide dynamic range, combined with the tight clustering of the healthy state, confirms the method's superior reliability in quantifying fault severity under high-pressure conditions.

4.2.4. Case study IV

In a systematic experimental investigation under extreme pressure, vibration signatures were acquired from the first cylinder of a hydraulic pump system subjected to incremental pressurization in 10 MPa steps up to 40 MPa. As illustrated in Fig. 41, time-domain signals at 40 MPa exhibited significant baseline shifts deviating from zero across all health states. Analogous to the 30 MPa waveforms, suction valve fault and discharge valve fault signals maintained waveform similarity, while dual valve fault signals manifested as complex pulse trains with alternating amplitude cycles, indicating extreme fault coupling under high pressure. Healthy condition signals displayed intense periodic oscillations interspersed with irregular minor impulses, reflecting heightened dynamic instability characteristic of the extreme-pressure regime.

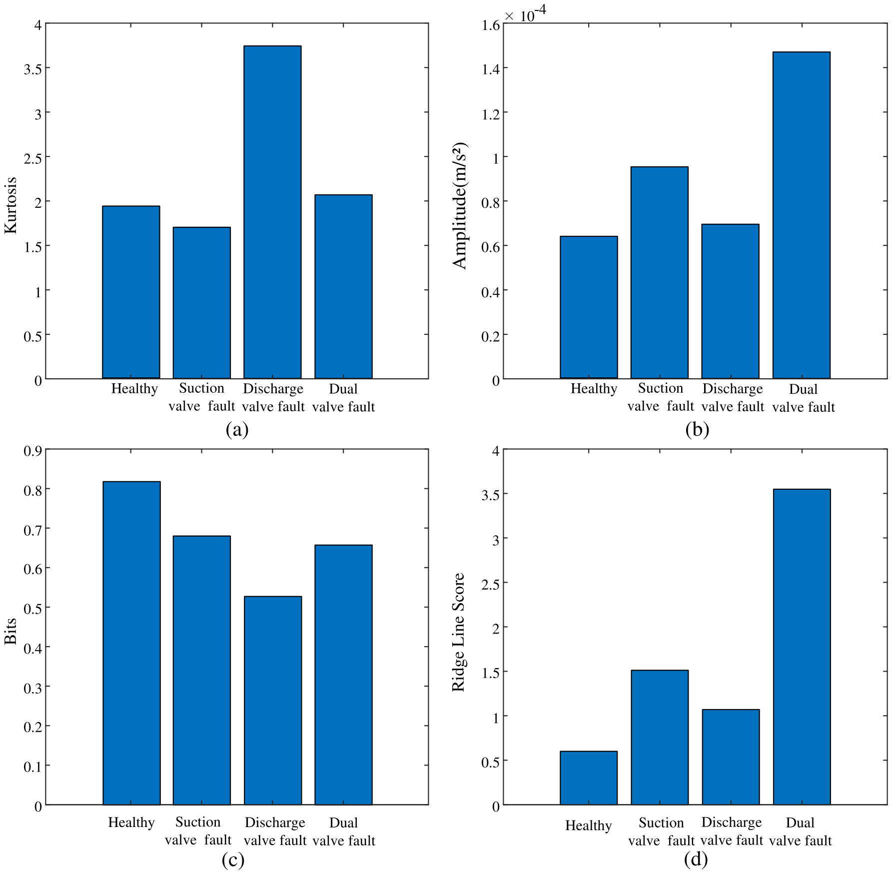

Fig. 36. Comparative analysis of diagnostic signals at 30 MPa. (a) Kurtosis (b) Local energy (c) Information entropy (d) Ridge line score.

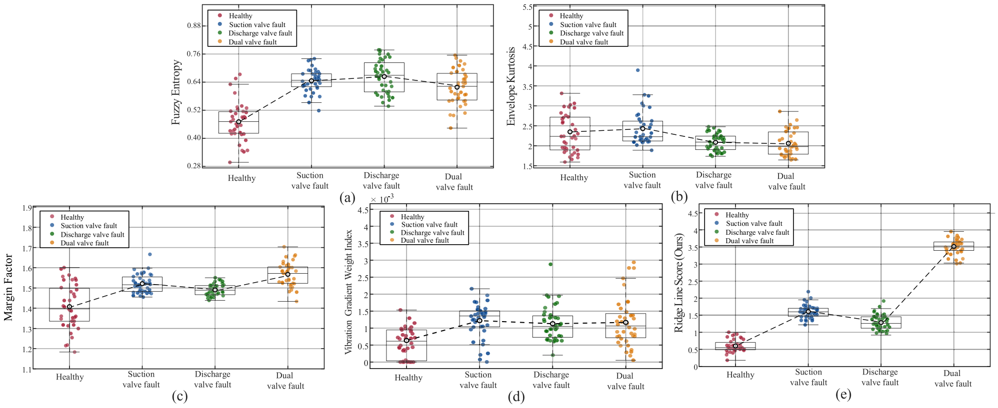

Fig. 37. Scatter plot comparison of fault indicators across four health states at 30 MPa: (a) Fuzzy Entropy (b) Envelope Kurtosis (c) Margin Factor (d) VGWI (e) The proposed method.

For the 40 MPa dataset, decomposed signals reveal unique IMF selection patterns distinct from low-pressure analyses, highlighting altered modal behaviors under extreme loading. Suction and discharge valve faults (Fig. 38(a), Fig. 38(b)) maintain similar energy ratio distributions across IMFs, predominantly concentrated in higher-order components, with most spectral kurtosis values remaining elevated. Notably, discharge valve faults exhibit spectral kurtosis approaching zero in IMF5, an aberration whose impact on the comprehensive ESK metric is negligible due to IMF5's low energy ratio. Healthy condition and dual valve fault signals show nearly identical energy concentration and kurtosis similarity, a feature attributed to intensified baseline oscillations driven

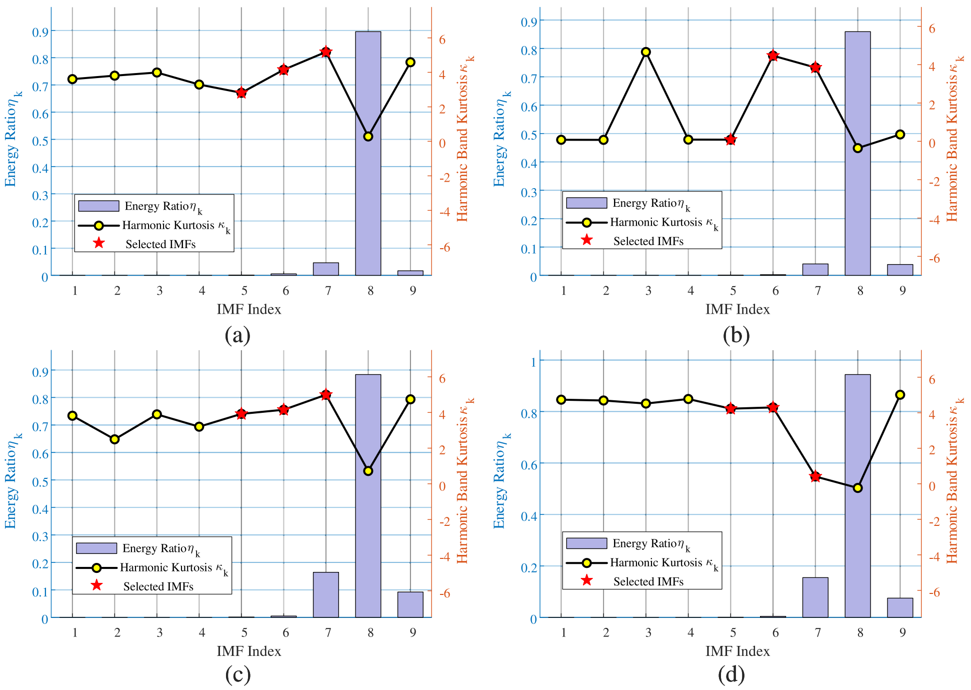

Fig. 38. IMF selection criteria analysis using energy ratio and kurtosis values: (a) Suction valve fault (b) Discharge valve fault (c) Healthy operation (d) Dual valve fault.

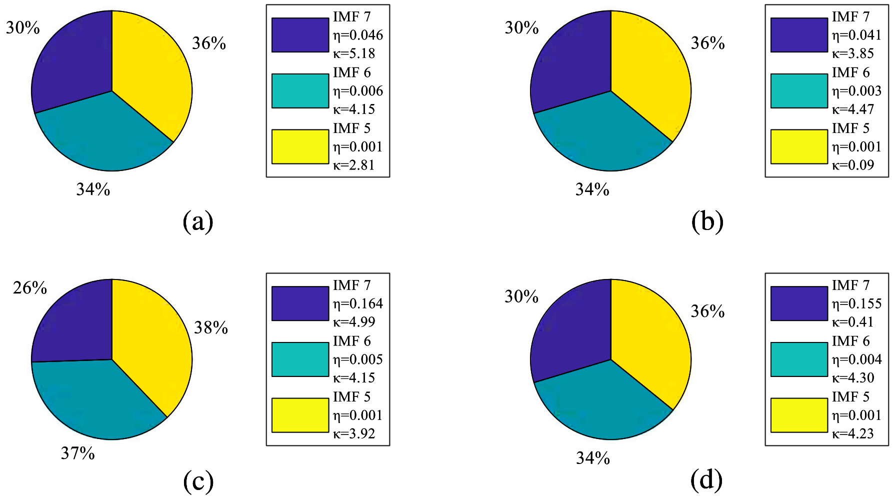

Fig. 39. Optimized weighting coefficients for IMF signal reconstruction: (a) Suction valve fault (b) Discharge valve fault (c) Healthy condition (d) Dual valve fault.

by extreme pressure-induced mechanical stress. Dual valve fault retains lower harmonic spectral kurtosis in IMF7, significantly influencing ESK weight calculations.

Optimized weighting coefficients for IMF signal reconstruction (Fig. 39) further validate this effect. As shown in Fig. 38(a), Fig. 38(b) and Fig. 38(d), all three fault types maintain identical weight distributions, while healthy conditions owing to high kurtosis values in IMF7 exhibit reversed ESK weights at lower levels, consistent with observed increases in high-frequency content and reductions in low-frequency baselines in time-domain signals. This adaptive weighting strategy effectively mitigates background noise, isolating subtle fault features amidst pronounced nonlinear distortions.

Crucially, to ensure algorithmic stability persists even in this extreme pressure regime, we analyzed the SNR variation across different mode numbers and penalty factors to investigate parameter dependence under the maximum load condition of 40 MPa.

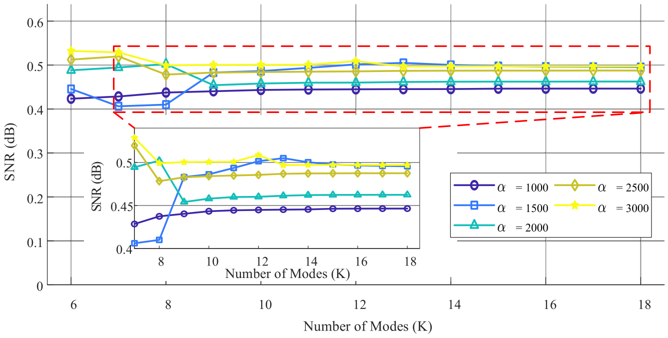

Fig. 40. Impact of mode number K and penalty factor α on the SNR of the reconstructed signal under 40 MPa.

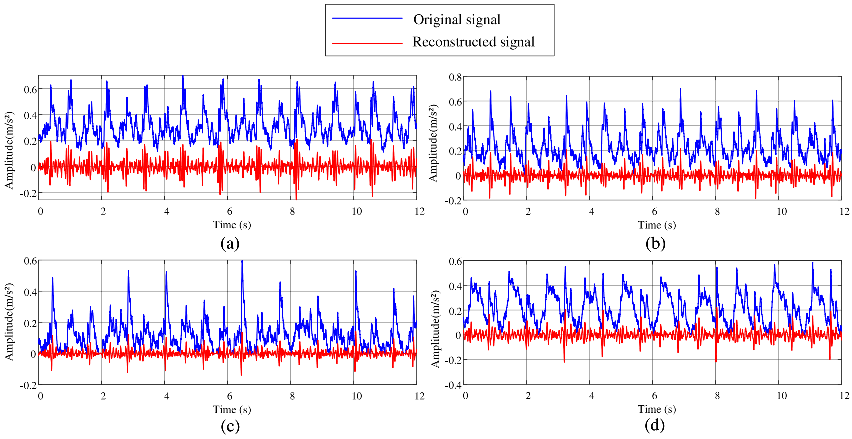

Fig. 41. Original versus reconstructed signals: (a) Suction valve fault (b) Discharge valve fault (c) Healthy condition (d) Dual valve fault.

As illustrated in Fig. 40, the SNR fluctuates within a narrow range with the increase of K when the value of K is relatively low. Nevertheless, all SNR curves tend to stabilize uniformly once $K \geq 9$. There are minor disparities among the curves of different penalty factors, and all such differences fall within an acceptable range. This confirms that the proposed framework maintains its reliability and effectiveness even under extreme operating conditions.

The comparative analysis of original and reconstructed signals in Fig. 41 elucidates pressure-driven fault evolution mechanisms under 40 MPa operating conditions. Although the reconstructed signals of suction and discharge valve faults retain temporal similarity, the former enhances the periodicity of high-frequency pulses and amplifies chaotic amplitude fluctuations, while the latter exhibits sharper impulsive patterns in periodic vibrations (Fig. 41(a), Fig. 41(b)). For dual valve faults, as shown in Fig. 41(d), the characteristic alternation between sustained high amplitude impacts and transient low energy intervals becomes significantly attenuated in reconstructions, confirming multi-source nonlinear fault coupling dynamics observed across multiple pressure regimes. The healthy condition (Fig. 41(c)) smooths most random noise, markedly improving the periodicity of the system's natural operational vibrations. Notably, all reconstructed fault signatures demonstrate intensified impulse distinctness, as the high-pressure environment amplifies previously obscured impact features within the time domain.

Complementary spectral evidence in Fig. 42 establishes pressure-dependent frequency response characteristics: fault signal energies consistently converge toward specific harmonic orders of the fundamental vibration frequency. In particular, the dual-valve fault (Fig. 42(d)) maintains high-magnitude responses across multiple orders, whereas the reconstructed signal of the healthy condition (Fig. 42(c)) shows only weak responses, forming a marked distinction from fault signals.

To visually corroborate these spectral characteristics in the time domain, Fig. 43 displays the signal reconstruction results for the maximum load condition of 40 MPa. Due to the intensified impact energy associated with the severe fault at this extreme pressure, all four comparative methods successfully capture high-amplitude fault impulses; however, the reconstruction quality varies significantly regarding waveform consistency and background purity. The proposed method (Fig. 43(a)) yields the superior result, distinguishing itself by maintaining the cleanest spectral baseline and the most uniform impulse morphology. In contrast, while the IMD method (Fig. 43(b)) correctly identifies the fault periodicity, it exhibits significant amplitude inconsistency, where the extracted impulse intensities fluctuate erratically rather than maintaining a stable physical magnitude. Similarly, although MCKD (Fig. 43(c)) and MOMEDA (Fig. 43(d)) effectively enhance the impulsive features, the extracted waveforms remain accompanied by noticeable residual background noise and spurious fluctuations between the main peaks. Under the extreme 40 MPa condition, while

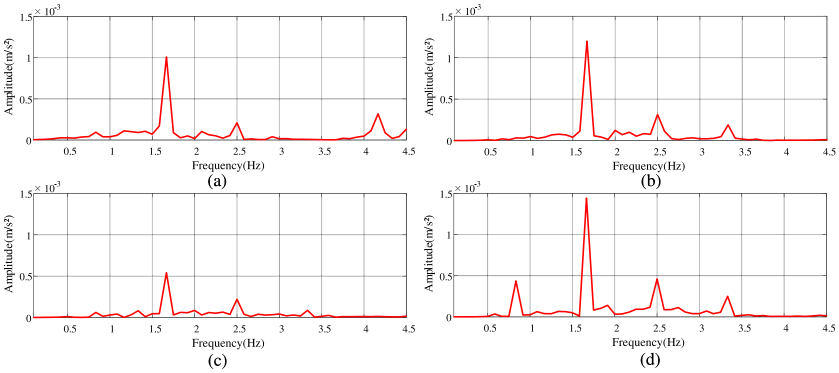

Fig. 42. Spectral analysis of reconstructed signals at 40 MPa: (a) Suction valve fault (b) Discharge valve fault (c) Healthy condition (d) Dual valve fault.

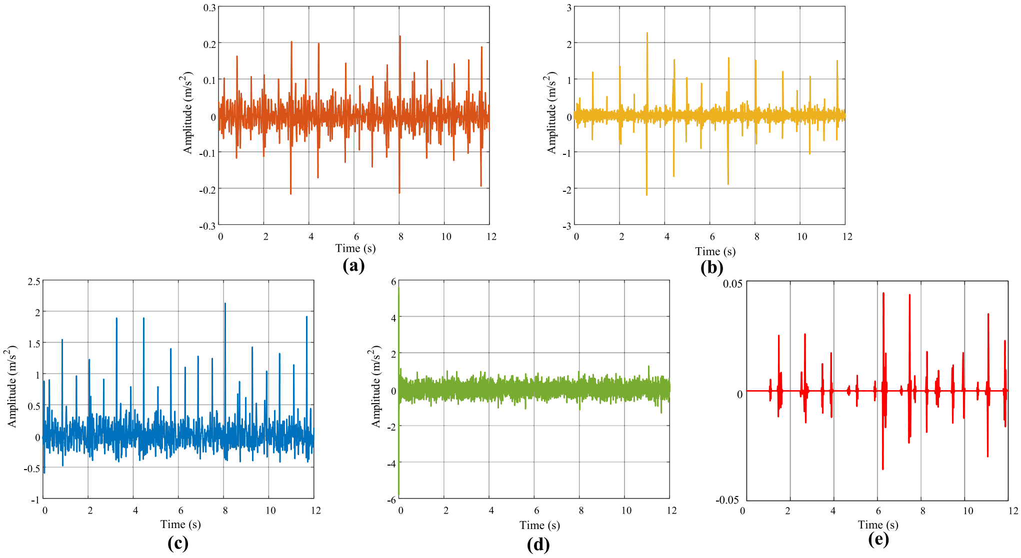

Fig. 43. Comparison of reconstructed time-domain signals at 40 MPa: (a) The proposed method (b) IMD (c) MCKD (d) MOMEDA (e) MTSK-HMMS-S.

the MTSK-HMMS-S method (Fig. 43(e)) still captures the fault's periodicity, its limitations in preserving nonlinear coupling dynamics are maximally exposed. The reconstructed signal exhibits extreme amplitude distortion, failing to reflect the alternating amplitude cycles inherent to the raw dual-valve fault. Extreme pressure environments induce severe baseline shifts and complex dynamic couplings that violate the algorithm's ideal constant-phase assumptions, proving that an inflexible temporal template is inadequate for characterizing compounded faults under extreme loads. Quantitative data in Table 1 conclusively confirms these limitations under extreme load. While MTSK-HMMS-S still forces a high NRR (96.45%) via rigid truncation, its Envelope SNR (ESNR) plummets to 0.2100 dB—significantly lower than the proposed method's 0.6337 dB. This drastic drop in envelope periodicity mathematically validates our visual observation: the inflexible temporal template causes severe amplitude distortion and fails to extract the true nonlinear coupling dynamics. The proposed method effectively mitigates these limitations, demonstrating superior robustness against high-pressure noise and extreme structural modulations compared to the evaluated baselines.

Feature domain construction under 40 MPa extreme pressure conditions reveals multiscale coupling patterns between fault and healthy states. The suction valve fault manifestation displays deeply interwoven energy concentrations between low-order harmonic bands and mid-high Walsh coefficient responses, forming dense energy clusters as demonstrated in Fig. 44(a). Discharge valve faults exhibit marginally lower energy amplitudes while maintaining analogous distribution patterns, observable in Fig. 44(b). Dual valve faults establish stepped energy configurations across full-order frequency bands, generating multiple continuous ridge lines under high-pressure environments evident in Fig. 44(d). Although healthy states preserve low-order energy baselines at 1.66 Hz, their low-amplitude expressions combined with fragmented Walsh-domain responses create discontinuous peak clusters visible in Fig. 44(c). Such disordered distributions simultaneously reflect superimposed natural vibration modes under extreme pressure and establish differentiable patterns from fault signals.

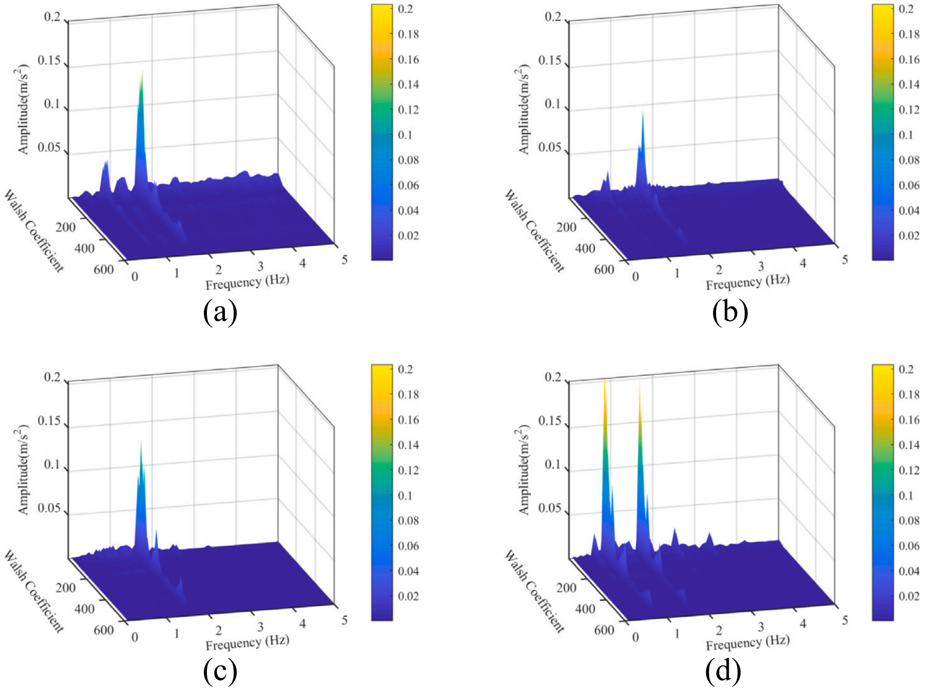

Fig. 44. 3D heatmap of the feature domain of the signals at 40 Mpa: (a) Suction valve fault (b) Discharge valve fault (c) Healthy condition (d) Dual valve fault.

The ridge distribution decodes the anisotropic propagation characteristics of faults under high voltage through a dynamic tracking mechanism. Suction valve fault ridge lines under extreme pressure exhibit frequent gradient direction mutations, driving continuous directional weight variations that reflect multidirectional energy propagation characteristics visualized in Fig. 45(a). Discharge valve fault ridges demonstrate fracture-reconstruction behavior where strong response regions trigger adaptive tracking step enlargement, accelerating ridge extension while frequently meeting direction-ambiguity termination conditions that disrupt propagation continuity, captured in Fig. 45(b). Dual valve faults conversely develop explicit geometric ridge distributions shown in Fig. 45(d), featuring broad ridges dominated by low-order frequency energy fusion, bifurcated ridges governed by high Walsh sequences, and compact directionally defined ridges regulated by high-order frequency bands. Healthy states yield fragmented ridge distributions induced by multimodal superposition and instability revealed in Fig. 45(c). Localized weak impacts enforce strict dual-criteria screening (local maxima, peak valley thresholds) that excludes pseudo peaks during initial feature point selection, resulting in sparse short ridge lines that align with theoretical tracking limitations for weak periodic components. The fault scoring model precisely quantifies this complex interplay through calculations of ridge line count, average length, and energy density, enabling reliable discrimination among homogeneous multisource faults.

Fig. 46 compares performance under extreme pressure conditions. Kurtosis and local energy fail to differentiate valve faults from the healthy baseline, as the high-pressure background noise obscures the fault impulses (Fig. 46(a)–(b)). Similarly, information entropy yields conflicting rankings for discharge faults due to signal complexity changes. In contrast, the ridge line score leverages multi-domain fusion to outperform traditional metrics. As shown in Fig. 46(d), dual valve faults achieve significantly higher scores than single faults, which in turn exceed healthy conditions by substantial margins, confirming reliable diagnostic differentiation even in high-noise environments.

Synthesizing the experimental results across the four pressure cases, the proposed method demonstrates distinct advantages over both conventional and state-of-the-art indicators. Regarding baseline stability and severity quantification, the proposed method exhibits exceptional robustness. Under low-pressure, high-noise conditions (10 MPa), the Ridge Line Score for healthy samples is essentially zero, and it remains consistently low even as pressure increases. More importantly, across all four pressure regimes, the method strictly adheres to a diagnostic hierarchy correlated with fault severity. Specifically, the metric values are lowest for Healthy samples, increase slightly for Discharge Valve Faults, rise further for Suction Valve Faults, and reach their peak for Dual Valve Faults. In contrast, while metrics like Kurtosis and Local Energy can distinguish healthy from faulty states in specific scenarios, they fail to differentiate the severity levels of the faults. Furthermore, Information Entropy fails to distinguish healthy from faulty states in the majority of operating conditions due to signal complexity overlaps. Finally, compared to the state-of-the-art research works listed in Table 2, the proposed method provides the clearest separation boundaries and the most stable clustering performance, confirming its superiority in complex mechanical diagnosis.

Concluding the quantitative evaluation, the comparative analysis for the 40 MPa case is shown in Fig. 47. Under this maximum pressure condition, the conventional metrics in panels (a) and (b) exhibit substantial overlap, failing to differentiate specific failure

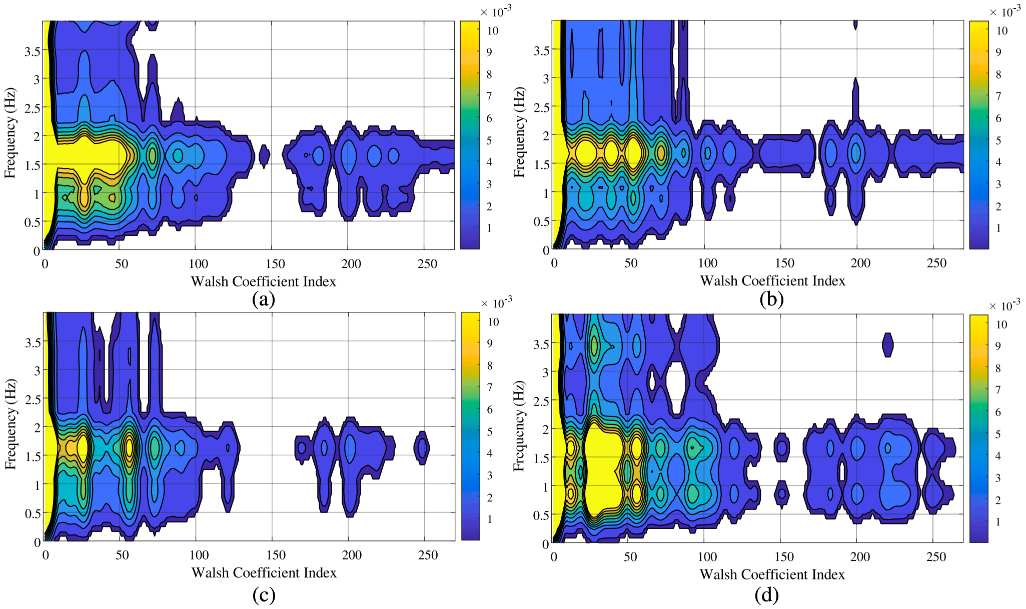

Fig. 45. Ridge-line distributions in feature domain at 40 MPa. (a) Suction valve fault (b) Discharge valve fault (c) Healthy condition (d) Dual valve fault.

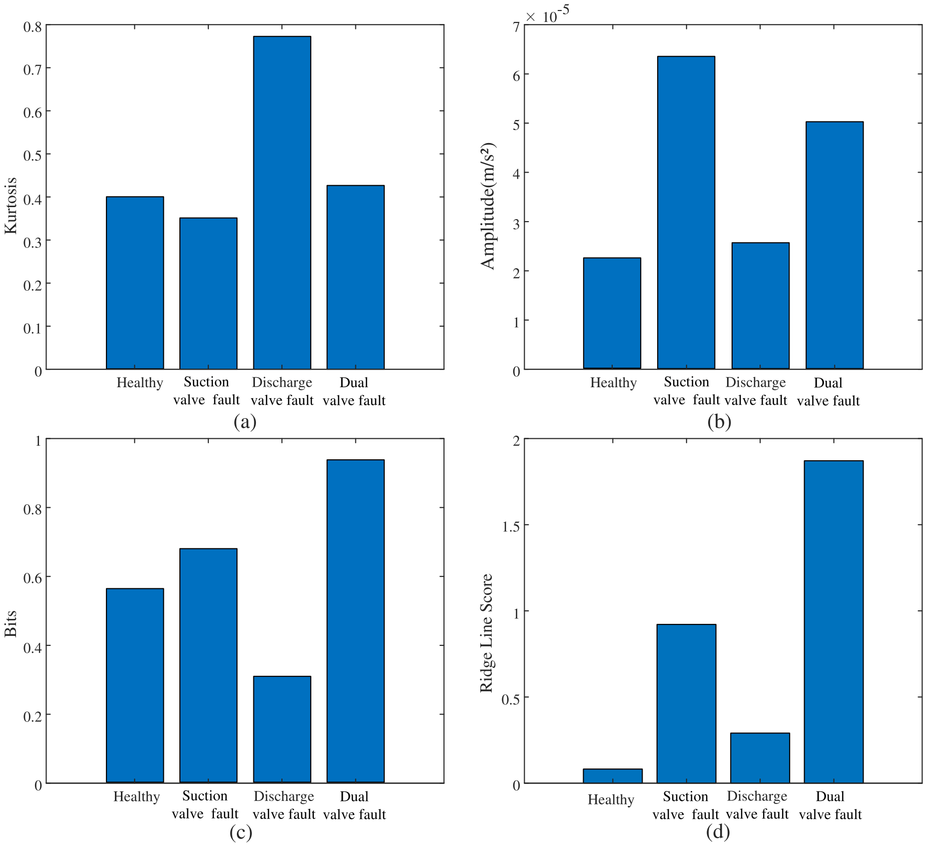

Fig. 46. Comparative analysis of diagnostic signals at 40 MPa. (a) Kurtosis (b) Local energy (c) Information entropy (d) Ridge line score.

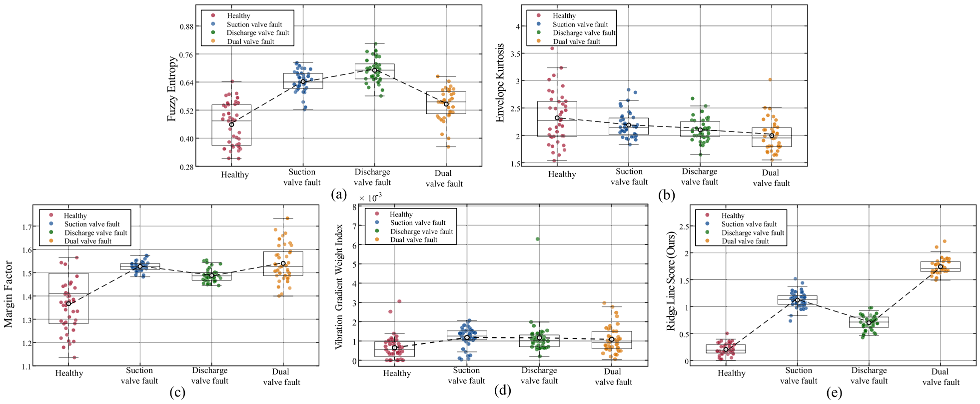

Fig. 47. Scatter plot comparison of fault indicators across four health states at 40 MPa: (a) Fuzzy Entropy (b) Envelope Kurtosis (c) Margin Factor (d) VGWI (e) The proposed method.

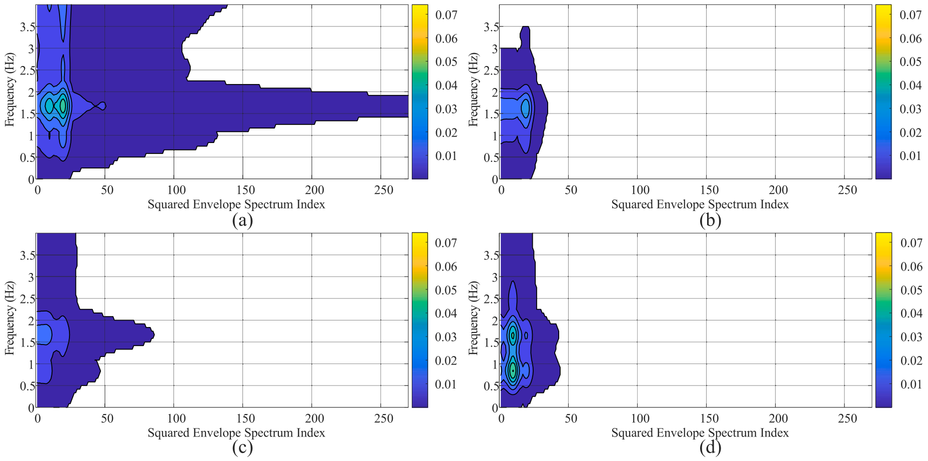

Fig. 48. Ridge-line distributions based on SES-FT joint representation in feature domain at 40 MPa. (a) Suction valve fault (b) Discharge valve fault (c) Healthy condition (d) Dual valve fault.

modes. In comparison, the methods in panels (c) and (d) show partial improvement. However, critical limitations persist: they fail to effectively assess the most severe dual valve fault condition. Specifically, VGWI (panel d) yields a score of 1.09 for the dual fault, which is anomalously lower than both single fault conditions (1.13 and 1.12), creating a high risk of underestimating fault severity under extreme pressure.

Conversely, the proposed method (Fig. 47(e)) overcomes these ambiguities, achieving distinct clustering with minimal variance. As detailed in Table 2, the metric values strictly follow the established severity hierarchy: lowest for the healthy state, increasing through discharge and suction faults, and peaking at the dual fault. This confirms that the diagnostic monotonicity and resolution of the proposed method remain robust up to the maximum operating pressure.

4.3. Ablation study:Justification and effectiveness of the Walsh–frequency joint representation

To rigorously justify the selection of the Walsh transform for constructing the hybrid feature domain, an ablation study was conducted comparing the proposed Walsh–frequency joint representation against two comparative joint domains. These baselines were constructed based on widely adopted signal processing transformations: the Squared Envelope Spectrum (SES) [42] and the Discrete Cosine Transform (DCT) [43]. To ensure a fair comparison, all three base transformations were equivalently coupled with the Fourier Transform (FT), mapping them into an identical two-dimensional feature space (yielding the SES-FT and DCT-FT representations, respectively). To intuitively demonstrate the spatial decoupling capabilities of these methods, we present the two-dimensional contour maps and ridge-line distributions extracted under the 40 MPa extreme pressure condition. This specific high-pressure regime is selected for visual analysis because the intensified background noise and severe mechanical coupling visually accentuate the representation differences among the methods.

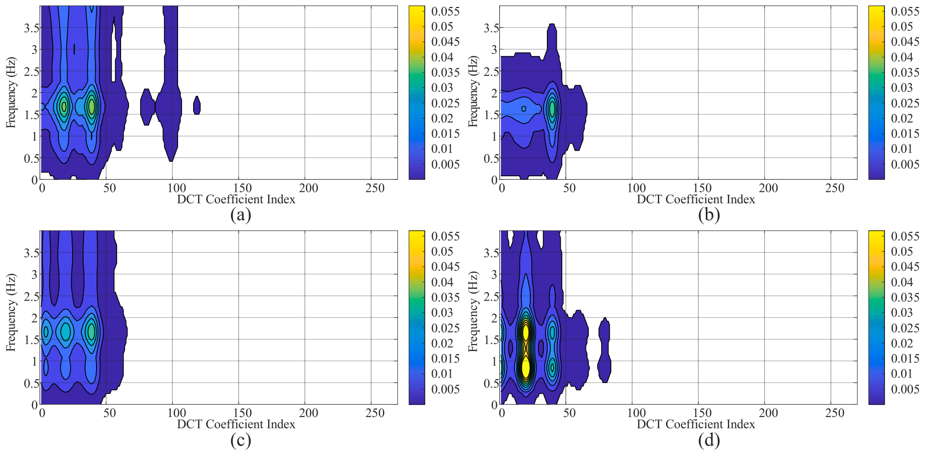

Fig. 49. Ridge-line distributions based on DCT-FT joint representation in feature domain at 40 MPa. (a) Suction valve fault (b) Discharge valve fault (c) Healthy condition (d) Dual valve fault.

Table 3
Comparison of ridge line scores extracted from DCT-FT, SES-FT, and Walsh-FT feature domains across varying discharge pressures.

Method	Health state	10 MPa	20 MPa	30 MPa	40 MPa
DCT-FT	Healthy	1.4501	4.3941	2.5690	1.3368
	Suction Fault	1.3014	1.3452	3.1416	0.9819
	Discharge Fault	0.7872	1.1150	3.0496	1.1829
	Dual Fault	0.0004	0.0224	0.9206	3.1374
SES-FT	Healthy	0.7693	4.9500	2.0907	0.7818
	Suction Fault	2.0463	1.7777	4.3039	0.6355
	Discharge Fault	0.7207	2.9428	1.6323	1.6533
	Dual Fault	3.2236	1.0417	1.2854	1.6135
Walsh-FT	Healthy	**0.0052**	**0.0977**	**0.6132**	**0.0819**
	Suction Fault	**0.9782**	**0.4082**	**1.5109**	**0.9215**
	Discharge Fault	**0.7236**	**0.2752**	**1.1815**	**0.2905**
	Dual Fault	**2.5042**	**0.7387**	**3.5806**	**1.8711**

As illustrated in Fig. 48, the SES-FT contour analysis suffers from severe spectral smearing. Moreover, its effective feature components are densely confined to a very narrow low-index range (typically under 100), leading to a severe lack of spatial resolution. The transient impact features merge into massive, continuous high-energy blocks, completely obliterating the sharp boundaries between different fault modes. This global aliasing effect renders the topological extraction of distinct ridge lines virtually impossible.

The DCT-FT contour maps shown in Fig. 49 demonstrate a slight improvement in energy compaction. However, because the underlying DCT relies on continuous cosine basis functions, it is fundamentally ill-suited for representing the sharp discontinuities of mechanical impacts. Similar to SES, the primary DCT coefficients are strictly squeezed into a narrow index range (under 100), which restricts the representation capacity for wide-band transient impacts. The extracted features manifest as elongated vertical bands with gradual gradients, which are insufficient to support robust directional ridge tracking.

In stark contrast, the proposed Walsh-FT contour maps (Fig. 45) map the signal into a highly sparse and discrete feature space, expanding the transient energy across a significantly broader and more resolved sequency index range. By utilizing rectangular basis functions that perfectly match abrupt impact transients without inducing the Gibbs phenomenon, the Walsh-FT representation isolates the fault energies into distinct, “island-like” geometric clusters with sharp gradient boundaries. This precise topological separation provides the necessary foundation for the dynamic ridge tracking algorithm.

To further substantiate these visual observations with quantitative evidence, we extracted the ridge line scores based on the feature domains generated by these three joint transformation methods across all four operating pressures (10 MPa to 40 MPa). The comparative results are summarized in Table 3.

An analysis of Table 3 reveals critical flaws in the conventional joint transformations when applied to homotypic multi-source diagnosis. The DCT-FT method severely mischaracterizes the system’s health states: at 10, 20, and 30 MPa, the baseline “Healthy” state paradoxically yields higher scores than actual single-valve faults. Furthermore, it completely fails to capture the severity of the dual fault at low pressures (scoring near-zero at 10 MPa and 20 MPa), violating the fundamental requirement of fault severity assessment.

Similarly, the SES-FT method exhibits chaotic, non-monotonic behavior. For instance, at 20 MPa, the healthy state records the highest score (4.9500) while the severe dual fault scores the lowest (1.0417). At 40 MPa, the suction fault (0.6355) is incorrectly scored lower than the healthy condition (0.7818). This erratic numerical distribution proves that continuous high-energy blocks in SES-FT heavily confound the dynamic tracking algorithm.

In contrast, the proposed Walsh-FT method guarantees both baseline stability and diagnostic monotonicity. Across all four pressure regimes, the healthy state consistently maintains the lowest score (near zero), providing a highly stable baseline. Meanwhile, the dual fault condition consistently registers the absolute highest score in every pressure category, reliably reflecting the compounded severity of multi-source impacts. This quantitative evidence conclusively validates that the Walsh–frequency joint representation offers a critical advantage in creating a mathematically robust feature domain capable of quantifying fault severity in multi-cylinder drilling pumps.

5. Conclusion

The development and implementation of the HMR-DHFT framework represents an advancement in the field of fault diagnosis for multi-cylinder drilling pump systems. Through the innovative integration of Walsh–frequency domain analysis and dynamic hierarchical feature tracing, this study has successfully addressed the longstanding challenges associated with homotypic multi-source mixing phenomena. Specifically, the mechanism-informed adaptive decomposition was proven to successfully isolate fault-related modes from background noise, eliminating the subjectivity of manual parameter tuning. Furthermore, the hybrid Walsh–frequency representation effectively resolved the spectral blurring issue, providing a high-contrast feature space where transient fault impulses remain distinguishable even when frequency bands overlap. Crucially, the matrix-free dynamic ridge tracking strategy exhibited superior robustness in data-scarce environments, enabling the precise extraction of fault evolution patterns without the complex mixing matrix estimation required by Blind Source Separation.

Experimental results validate the superior performance of the proposed methodology, exhibiting comprehensive improvements in diagnostic resolution and severity quantification across varying pressure regimes when compared to conventional enhancement methods and recent domain-specific baselines. The success of this framework opens new avenues for future research in automated fault diagnosis systems, particularly in complex industrial applications where signal mixing and interference pose significant challenges. Despite these promising results, it is important to acknowledge the limitations of the current study. The experimental validation is restricted to a single machine type (a specific multi-cylinder drilling pump) using a fixed hybrid sensor arrangement, and the evaluated dataset is limited to a single rotational speed (50 SPM) under varying discharge pressures. Consequently, the applicability and generalizability of the HMR-DHFT framework under alternative sensor arrangements and a broader set of operating conditions require further rigorous experimental verification. Furthermore, while the foundational concept of Walsh–frequency fusion can be migrated to other equipment, direct application is insufficient. Due to fundamental differences in mechanical structures and dynamic behaviors, extending this framework to new domains necessitates specific, targeted optimizations of the signal processing pipeline tailored to the target equipment's unique characteristics. Furthermore, the current study was conducted without explicitly modeling or parameterizing the influence of uncontrolled ambient temperature fluctuations. Therefore, future work will focus on validating the framework across diverse machine types, variable speed regimes, and alternative sensor configurations, alongside incorporating environmental compensation mechanisms and edge computing integration for comprehensive online health monitoring.

CRediT authorship contribution statement

Peng Chen: Writing – review & editing, Writing – original draft, Supervision, Software, Resources, Project administration, Methodology, Investigation, Funding acquisition, Conceptualization. **Yazheng Wang:** Visualization, Validation, Software, Methodology, Formal analysis, Data curation, Conceptualization. **Yuhao Wu:** Writing – original draft, Visualization, Validation, Software, Resources, Methodology, Investigation, Formal analysis, Data curation, Conceptualization. **Yaqiang Jin:** Supervision, Resources, Project administration, Funding acquisition, Conceptualization. **Changbo He:** Supervision, Project administration, Funding acquisition, Formal analysis, Conceptualization. **Ge Xin:** Supervision, Project administration, Funding acquisition.

Declaration of competing interest

The authors declare that they have no known competing financial interests or personal relationships that could have appeared to influence the work reported in this paper.

Acknowledgments

This research was supported by the National Natural Science Foundation of China (Grants 52105111 and 52305085) and the Guangdong Basic and Applied Basic Research Foundation (Grant 2025A1515012256).

Data availability

Data will be made available on request.

References

[1] K. Fang, L. Tong, X. Xu, J. Cai, X. Peng, M. Omar, A.K. Bashir, W. Wang, Robust fault diagnosis of drilling machinery under complex working conditions based on carbon intelligent industrial internet of things, IEEE Internet Things J. (2025) 1–1.

[2] J. Guo, Y. Yang, H. Li, L. Dai, B. Huang, A parallel deep neural network for intelligent fault diagnosis of drilling pumps, Eng. Appl. Artif. Intell. 133 (2024) 108071.

[3] G. Li, J. Hu, Y. Ding, A. Tang, J. Ao, D. Hu, Y. Liu, A novel method for fault diagnosis of fluid end of drilling pump under complex working conditions, Reliab. Eng. Syst. Saf. 248 (2024) 110145.

[4] P. Chen, R. Zhang, S. Fan, J. Guo, X. Yang, Step-wise contrastive representation learning for diagnosing unknown defective categories in planetary gearboxes, Knowl.-Based Syst. 309 (2024) 112863.

[5] J. Guo, Y. Yang, H. Li, J. Wang, A. Tang, D. Shan, B. Huang, A hybrid deep learning model towards fault diagnosis of drilling pump, Appl. Energy 372 (2024) 123773.

[6] P. Chen, Y. Wu, J. Ma, R. Zhang, G. Xin, C. He, Vibration-weighted maximum correlated kurtosis deconvolution and latent cyclic pattern discovery for fault diagnosis of high-speed rail bogies, J. Sound Vib. (2026) 119657.

[7] P. Chen, J. Gao, Y. Wu, C. He, G. Xin, S. Fan, J. Qi, Semi-supervised transfer graph representation learning with few-shot adaptation for gearbox diagnostics under extraneous transient noise, Struct. Health Monit. (2026) 14759217251414344.

[8] D.-T. Nguyen, T.-P. Nguyen, M.-Y. Cho, Cloud-based aIoT intelligent infrastructure for firefighting pump fault diagnosis-based hybrid CNN-GRU deep learning technique, J. Supercomput. 81 (3) (2025) 462.

[9] P. Chen, R. Zhang, C. He, Y. Jin, S. Fan, Progressive contrastive representation learning for defect diagnosis in aluminum disk substrates with a bio-inspired vision sensor, Expert Syst. Appl. 289 (2025) 128305.

[10] P. Chen, Y. Wu, S. Fan, C. He, Y. Jin, J. Qi, C. Zhou, Adaptive signal regime for identifying transient shifts: A novel approach toward fault diagnosis in wind turbine systems, Ocean Eng. 325 (2025) 120798.

[11] P. Chen, J. Ma, J. Gao, G. Xin, C. He, Markovian spectral transition modeling with temporal dependencies for railway bogie axle bearing diagnostics in non-stationary transient environments, Nonlinear Dynam. 114 (2026) 244.

[12] P. Chen, Y. Wu, C. Xu, Y. Jin, C. Zhou, Markov modeling of signal condition transitions for bearing diagnostics under external interference conditions, IEEE Trans. Instrum. Meas. 73 (3518308) (2024).

[13] M. Omidali, M. Khazaee, M. Jahromi, A.M. Dizgoini, Comprehensive review on fault diagnostics and isolation methods for piston engines regarding monitoring of reciprocating equipment, J. Therm. Anal. Calorim. 150 (2025) 16911–16937.

[14] L. Debnath, F.A. Shah, Wavelet Transforms and Their Applications, vol. 434, Springer, 2015.

[15] P. Flandrin, G. Rilling, P. Goncalves, Empirical mode decomposition as a filter bank, IEEE Signal Process. Lett. 11 (2) (2004) 112–114.

[16] K. Dragomiretskiy, D. Zosso, Variational mode decomposition, IEEE Trans. Signal Process. 62 (3) (2013) 531–544.

[17] B. Hou, M. Xie, H. Yan, D. Wang, Impulsive mode decomposition, Mech. Syst. Signal Process. 211 (2024) 111227.

[18] P. Chen, Y. Wu, C. Xu, C.-G. Huang, M. Zhang, J. Yuan, Interference suppression of nonstationary signals for bearing diagnosis under transient noise measurements, IEEE Trans. Reliab. (2025) 1–15.

[19] P. Chen, K. Wang, M.J. Zuo, D. Wei, An ameliorated synchroextracting transform based on upgraded local instantaneous frequency approximation, Measurement 148 (2019) 106953.

[20] D. Wu, Y. Wang, P. Chen, C. Guo, R. Li, G. Xin, C. He, Cross-correlation heat-maps synthesis with walsh-Fourier transformation in articulated robotic systems diagnostics, Measurement (2026) 120862.

[21] J. Zhang, G.P. Rangaiah, L. Dong, L. Samavedham, An improved industrial fault diagnosis model by integrating enhanced variational mode decomposition with sparse process monitoring method, Reliab. Eng. Syst. Saf. 253 (2025) 110492.

[22] A. Yang, M. Wu, C. Lu, W. Yu, J. Hu, Y. Nakanishi, Decision fusion scheme based on mode decomposition and evidence theory for fault diagnosis of drilling process, IEEE Trans. Ind. Inform. 20 (2) (2023) 2017–2028.

[23] G. Li, J. Hu, D. Shan, J. Ao, B. Huang, Z. Huang, A CNN model based on innovative expansion operation improving the fault diagnosis accuracy of drilling pump fluid end, Mech. Syst. Signal Process. 187 (2023) 109974.

[24] J. Guo, J.-L. Wan, Y. Yang, L. Dai, A. Tang, B. Huang, F. Zhang, H. Li, A deep feature learning method for remaining useful life prediction of drilling pumps, Energy 282 (2023) 128442.

[25] Z. Li, Z. Liu, M. Zuo, Homotypic multi-source mixed signal decomposition based on maximum time-shift kurtosis for drilling pump fault diagnosis, Mech. Syst. Signal Process. 221 (2024) 111724.

[26] Y. Zhang, B. Han, M. Han, Mechanical fault diagnosis with noisy multisource signals via unified pinball loss intuitionistic fuzzy support tensor machine, IEEE Trans. Ind. Inform. 20 (1) (2024) 62–72.

[27] Z. Xu, K. Zhao, J. Wang, M. Bashir, Physics-informed probabilistic deep network with interpretable mechanism for trustworthy mechanical fault diagnosis, Adv. Eng. Inform. 62 (2024) 102806.

[28] Y. Miao, C. Li, B. Zhang, J. Lin, Application of a coarse-to-fine minimum entropy deconvolution method for rotating machines fault detection, Mech. Syst. Signal Process. 198 (2023) 110431.

[29] Y. Miao, C. Li, H. Shi, T. Han, Deep network-based maximum correlated kurtosis deconvolution: A novel deep deconvolution for bearing fault diagnosis, Mech. Syst. Signal Process. 189 (2023) 110110.

[30] J. Guo, Z. Si, J. Xiang, Cycle kurtosis entropy guided symplectic geometry mode decomposition for detecting faults in rotating machinery, ISA Trans. 138 (2023) 546–561.

[31] Y. Lu, Z. Yao, Q. Gao, D. Zhu, D. Zhao, D. Huang, A novel fault diagnosis method for bearing based on maximum average kurtosis morphological deconvolution, Meas. Sci. Technol. 35 (11) (2024) 116137.

[32] Q. Gao, H. Tang, J. Xiang, Y. Zhong, S. Ye, J. Pang, A walsh transform-based teager energy operator demodulation method to detect faults in axial piston pumps, Measurement 134 (2019) 293–306.

[33] Q. Zhang, X. Liu, T. Li, J. Shi, C.-H. Tan, X. Zhang, T. Shi, J. Xuan, Inference and quantification of cyclostationary impulses: A novel noise-sensitive mixed Gaussian cyclostationary model for compound fault detection, Mech. Syst. Signal Process. 229 (2025) 112501.

[34] G.L. McDonald, Q. Zhao, Multipoint optimal minimum entropy deconvolution and convolution fix: Application to vibration fault detection, Mech. Syst. Signal Process. 82 (2017) 461–477.

[35] J. Cheng, H. Pan, J. Zheng, Maximum Ramanujan spectrum signal-to-noise ratio deconvolution method: algorithm and applications, IEEE Trans. Ind. Inform. 20 (10) (2024) 11977–11986.

[36] L. Xu, H. Ni, Y. Zhang, D. Sun, Y. Zheng, M. Hu, Porous asphalt mixture use asphalt rubber binders: Preparation and noise reduction evaluation, J. Clean. Prod. 376 (2022) 134119.

[37] R. Yao, H. Jiang, C. Yang, H. Zhu, C. Liu, An integrated framework via key-spectrum entropy and statistical properties for bearing dynamic health monitoring and performance degradation assessment, Mech. Syst. Signal Process. 187 (2023) 109955.

[38] Z. Wang, H. Chen, Z. Yuan, J. Wan, T. Li, Multiscale fuzzy entropy-based feature selection, IEEE Trans. Fuzzy Syst. 31 (9) (2023) 3248–3262.

[39] Y. Li, S. Wang, Y. Yang, Z. Deng, Multiscale symbolic fuzzy entropy: An entropy denoising method for weak feature extraction of rotating machinery, Mech. Syst. Signal Process. 162 (2022) 108052.
[40] L. Hua, X. Wu, T. Liu, S. Li, The methodology of modified frequency band envelope kurtosis for bearing fault diagnosis, IEEE Trans. Ind. Inform. 19 (3) (2022) 2856–2865.
[41] W. Teng, W. Wang, H. Ma, Y. Liu, Z. Ma, H. Mu, Adaptive fault detection of the bearing in wind turbine generators using parameterless empirical wavelet transform and margin factor, J. Vib. Control 25 (6) (2019) 1263–1278.
[42] F. Lu, Q. Tong, X. Jiang, S. Du, J. Xu, J. Huo, Z. Zhang, Envelope spectrum neural network with adaptive domain weight harmonization for intelligent bearing fault diagnosis under cross-machine scenarios, Adv. Eng. Inform. 62 (2024) 102787.
[43] S.A. Nawaz, J. Li, D. Li, M.U. Shoukat, U.A. Bhatti, M.A. Raza, Medical image zero watermarking algorithm based on dual-tree complex wavelet transform, AlexNet and discrete cosine transform, Appl. Soft Comput. 169 (2025) 112556.